JGR Space Physics

RESEARCH ARTICLE
10.1029/2019JA026580

**Key Points:**
- A four-plasma classification scheme was used to separate the solar wind passing ACE into four types, and the four types were separately analyzed
- Significant systematic differences were found in the properties of solar wind fluctuations between the four types of plasma
- The authors recommend using a plasma classification scheme rather than a "slow wind" versus "fast wind" separation of solar wind data

**Correspondence to:**
J. E. Borovsky,
jborovsky@spacescience.org

**Citation:**
Borovsky, J. E., Denton, M. H., & Smith, C. W. (2019). Some properties of the solar wind turbulence at 1 AU statistically examined in the different types of solar wind plasma. *Journal of Geophysical Research: Space Physics*, *124*, 2406–2424. https://doi.org/10.1029/2019JA026580

Received 31 JAN 2019
Accepted 1 APR 2019
Accepted article online 10 APR 2019
Published online 29 APR 2019



# Some Properties of the Solar Wind Turbulence at 1 AU Statistically Examined in the Different Types of Solar Wind Plasma

**Joseph E. Borovsky[1], Michael H. Denton[1], and Charles W. Smith[2]**

[1]Center for Space Plasma Physics, Space Science Institute, Boulder, CO, USA, [2]Physics Department and Space Science Center, University of New Hampshire, Durham, NH, USA

**Abstract** A four-plasma classification scheme is used to categorize the ACE solar wind data set into four types of plasma: (1) coronal-hole-origin plasma, (2) streamer-belt-origin plasma, (3) sector-reversal-region plasma, and (4) ejecta. The statistical properties of the solar wind fluctuations at 1 AU are analyzed for each of the four types of plasma in the years 1998–2008 using ACE magnetic field and plasma measurements. Between the four types of solar wind plasma there are subtle statistical differences in the spectral indices of (a) trace-B, (b) trace-v, (c) total energy, (d) magnetic intensity, and (e) plasma number density. Between the four types of plasma there are significant statistical differences (a) in the Elsässer inward and outward spectral indices, (b) in the outward imbalance, (c) in the Alfvénicity, (d) in the normalized vector-B, vector-v, magnetic intensity, and number density fluctuation amplitudes, (e) in the population of strong current sheets, (f) in the population of sudden velocity shears, (g) in the anisotropies of magnetic field and velocity fluctuations, and (h) in the parallel-to-B magnetic field fluctuation spectral index. It is argued that the four-plasma categorization scheme is superior to a slow-versus-fast categorization for the study of turbulence and fluctuations in the solar wind.

## 1. Introduction

There are distinctly different types of solar wind plasma that emanate from different types of features on the solar surface (e.g., Cranmer et al., 2017; Crooker et al., 2014; Luhmann et al., 2013). Xu and Borovsky (2015) recently developed an algebraic four-plasma categorization scheme for the solar wind at 1 AU based on the measured properties of the plasma and magnetic field strength. The four types of plasma are (i) coronal-hole-origin plasma, (ii) streamer-belt-origin plasma, (iii) sector-reversal-region plasma, and (iv) ejecta. Note that "ejecta" here includes magnetic clouds, plus other (e.g., Cane & Richardson, 2003; Richardson & Cane, 2010) noncloud plasma. Note also that this algebraic scheme includes the separate categorization of plasma associated with streamer stalks (sector-reversal-region plasma; e.g., Foullon et al., 2011; Gosling et al., 1981; Ko et al., 2018; Suess et al., 2009; Susino et al., 2008). It is important to note that sector-reversal-region plasma is not synonymous with the "heliospheric plasma sheet"; the heliospheric plasma sheet is identified by high plasma density and high plasma beta (cf. Bavassano et al., 1997; Crooker et al., 2004; Winterhalter et al., 1994) whereas the sector-reversal-region plasma was originally identified via the electron strahl (cf. Xu & Borovsky, 2015). The sector-reversal-region plasma includes the heliospheric plasma sheet, but it is considerably broader. The Xu and Borovsky algebraic selection is based on the values of the proton number density $n_p$, the wind speed $v_{sw}$, the proton temperature $T_p$, and the magnetic field strength $B_{mag}$ in the solar wind, organized into three solar wind parameters: the proton specific entropy $S_p = T_p/n_p^{2/3}$, the temperature-to-speed ratio $T_p/v_{sw}$, and the Alfvén speed $v_A = B_{mag}/(4\pi m_p n_p)^{1/2}$ based upon the proton number density. (Note that $S_p$ and $v_A$ are the dominant deciders in this categorization (cf. Figure 3 of Xu & Borovsky, 2015), with the $T_p/v_{sw}$ value being less influential. The Xu and Borovsky categorization scheme is known as 3D4CAT, for the three-dimensional ($S_p$, $v_A$, and $T_p/v_{sw}$) algebraic scheme to divide the solar wind into four plasma categories. Camporeale et al. (2017) used a machine-learning technique called Gaussian Process to build a second four-plasma categorization scheme based on seven measured parameters: $v_{sw}$, $S_p$, $v_A$, $T_p$, the standard deviation of proton temperature values $\sigma T_p$, the 10.7-cm radio flux from the sun F10.7, and the sunspot number $R$. The Camporeale categorization scheme also rates the confidence level of the categorization. The Camporeale high-confidence categorization scheme provides a more accurately categorized

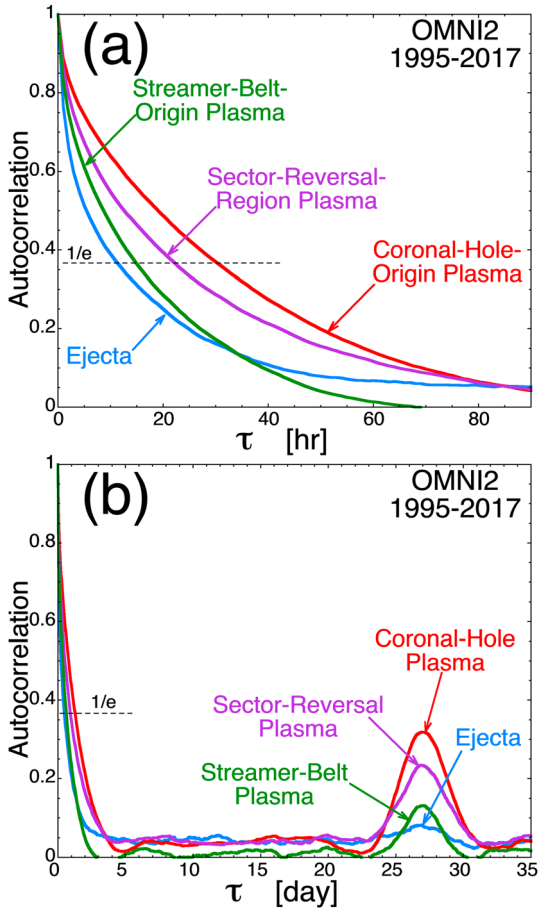


**Figure 1.** Autocorrelation functions for the occurrence of the four different types of solar wind plasma at 1 AU in the years 1995–2007 using the 1-hr-resolution OMNI2 data set. (a) From 0 to 90 hr and (b) from 0 to 35 days. As in all figures, red pertains to coronal-hole-origin plasma, green pertains to streamer-belt-origin plasma, purple pertains to sector-reversal-region plasma, and blue pertains to ejecta.

database than the Xu and Borovsky algebraic scheme does, but the Camporeale high-confidence scheme does not categorize all of the solar wind. (Low-confidence categorizations are removed from the data.)

Note that there are also three-plasma categorization schemes for the solar wind at 1 AU in the literature (Neugebauer et al., 2016): the three-plasma schemes in the literature are variously based on (1) the alpha-to-proton density ratio, the strength of the bidirectional electron strahl, the proton temperature, and the solar wind speed (Neugebauer et al., 2003; Reisenfeld et al., 2003), (2) the $O^{7+}/O^{6+}$ number-density ratio and $v_{sw}$ (Zhao et al., 2009), and (3) $S_p$ and $v_A$ (Figure 3 of Xu & Borovsky, 2015). Additionally, there are schemes to separately identify ejecta (e.g., Elliott et al., 2005; Gosling et al., 1973, 1987; Lepping et al., 2005; Richardson & Cane, 1995; Skoug et al., 2000). A comparison of the Neugebauer et al. (2003) three-plasma scheme, the Zhao et al. (2009) three-plasma scheme, and the Xu and Borovsky (2015) four-plasma scheme can be found in Neugebauer et al. (2016); the simultaneous agreement between the three schemes was only 49%. There has also been exploration of in situ solar wind measurements at ~0.3 AU to determine the origin of solar wind plasma; Stansby et al. (2018) used the measured proton temperature anisotropy and the measured cross helicity to determine plasma that originated from (a) the central portions of coronal holes versus (b) plasma from active regions or the edges of coronal holes versus (c) plasma from transients from streamers and pseudostreamers.

The Xu and Borovsky 3D4CAT categorization scheme will be used in this study; comparisons of the study results with the Camporeale high-confidence categorization show no significant changes. Where possible, the analysis of the present study is compared with the earlier analysis of Borovsky (2012a) using the Zhao et al. (2009) categorization scheme. Throughout this report the plotting color scheme will be (i) red for coronal-hole-origin plasma, (ii) green for streamer-belt-origin plasma, (iii) purple for sector-reversal-region plasma, and (iv) blue for ejecta.

Autocorrelation functions for the identification of the four types of plasma in the OMNI2 data set are plotted in Figure 1. The autocorrelation function $A(\tau)$ of a function $f(t)$ is constructed by first subtracting the average value of the function $f_o = \langle f(t) \rangle$ to produce a new function $F(t) = f(t) - f_o$; the autocorrelation function $A(\tau)$ of $f(t)$ is then $A(\tau) = \int F(t)F(t-\tau)\,dt / \int F(t)F(t)dt$. OMNI2 data from 1995–2017 are used because solar wind measurements became approximately continuous beginning in 1995. The autocorrelation times (1/*e* method in Figure 1a) for plasma type are on the order of 11 hr for ejecta, 30 hr for coronal-hole-origin plasma, 15 hr for streamer-belt-origin plasma, and 22 hr for sector-reversal-region plasma. These autocorrelation times are the typical durations of intervals of the various types of plasma as seen at 1 AU. Hence, the plasma type at 1 AU tends to change in a fraction of a day. Note in Figure 1b the recurrence probability of each type of plasma after the 27-day rotation period of the Sun as seen by the Earth, with ejecta (being impulsively emitted from the Sun) having only a very weak enhancement of its autocorrelation function at 27 days.

The plasma, heavy ion, magnetic field, and electron strahl properties of the solar wind are statistically different in the four types of solar wind plasma (Borovsky, 2018; Xu & Borovsky, 2015). Because of these statistical differences, temporal changes from one type of plasma to another as the structured solar wind advects past a measuring spacecraft produce many of the well-known temporal intercorrelations between solar wind variables at 1 AU (Borovsky, 2018). Systematic differences in the properties of the solar wind with phase of the solar cycle are also produced by changes in the occurrence rates of the four plasma types during the different phases of the solar cycle. The purpose of this study is to demonstrate that there are also systematic differences in the properties of the solar wind fluctuations in the four types of solar wind plasma.

This manuscript is organized as follows. In section 2 the data sets utilized for the study are discussed and the locations of the data are pointed out for the reader. In section 3 some plasma properties of relevance for turbulence studies are statistically examined for the four types of solar wind plasma. In section 4 the spectral indices of the vector velocity and vector magnetic field fluctuations of the solar wind are investigated. In section 5 the amplitudes of the vector velocity and vector magnetic field fluctuations are examined. In section 6 the statistical properties of current sheets and velocity shear layers in the solar wind are examined for the four types of plasma. In section 7 the Alfvénicity of the solar wind velocity and magnetic-field fluctuations is examined. In section 8 the component magnetic and component velocity spectral indices are examined in the Belcher and Davis (1971) magnetic coordinate system for the four types of plasma. In section 9 the anisotropies of the magnetic and velocity fluctuations are examined. In section 10 the magnetic field strength and proton number-density fluctuations of the solar wind are statistically examined for the four types of solar wind plasma. Section 11 contains a summary of the findings of this study. Section 12 contains a discussion about the merits of using the four-plasma categorization scheme instead of separating the solar wind into "slow" versus "fast".

## 2. The Data Sets

For the analysis of turbulence in the solar wind at 1 AU, data from two instruments onboard the ACE spacecraft upstream of the Earth are used: magnetic field measurements time averaged to 64-s time resolution from the Magnetic Field Instrument (Smith et al., 1998) and plasma and flow measurements with 64-s time resolution from the Solar Wind Electron Proton Alpha Monitor (McComas et al., 1998). All measurements used are from the "Merged IMF and Solar Wind 64-second Averages" ACE data set (available from the ACE Science Center at http://www.srl.caltech.edu/ACE/ASC/level2/index.html).

For higher-frequency analysis ($1.4 \times 10^{-3}$ to $1.6 \times 10^{-2}$ Hz, which corresponds to periods of 64 s to 12 min) the Level 3 "ACE Hourly Data Parameters for Magnetospheric Driving" data set available at http://www.ssg.sr.unh.edu/mag/ace/HourlyParms/HourlyParms.html in the ACE Science Data Center will be used. This data set contains a fluctuation analysis of 1-hr intervals of the ACE data set for the years 1998–2008 in the downloadable data file THA.out. This analysis obtains fitted spectral slopes from second-order structure functions. Fluctuation amplitudes corresponding to the $1.4 \times 10^{-3}$ to $1.6 \times 10^{-2}$ Hz frequency range are root-mean-square (rms) values of a 1-hr-long time series.

For lower-frequency analysis ($4.3 \times 10^{-4}$ to $1.9 \times 10^{-3}$ Hz, which corresponds to periods of 8.8–38.8 min) the analysis methodology of Borovsky (2012a) is used. This methodology uses 4.5-hr-long intervals (256 data points at 64-s resolution) of the "Merged IMF and Solar Wind 64-second Averages" ACE data. In categorizing each 4.5-hr interval according to the four types of plasma, unless all hours of a 4.5-hr interval obtain the same plasma categorization, that interval is deemed "not uniquely categorized" and is not used in the present study. This analysis obtains fitted spectral slopes from fast Fourier transform periodograms. The least-squares linear fits in log (power)-log (frequency) space utilize all of the periodogram data in the frequency interval $4.3 \times 10^{-4}$ to $1.9 \times 10^{-3}$ Hz; this differs from the least-squares fit method suggested by Podesta (2016) wherein the available periodogram data are interpolated onto a uniformly spaced grid in log (frequency) and the grid points are then used for the least-squares fit. Fluctuation amplitudes corresponding to the $4.3 \times 10^{-4}$ to $1.9 \times 10^{-3}$ Hz frequency range are rms values of a Fourier-filtered 4.5-hr-long time series.

In section 3 where some plasma properties of interest to turbulence analysis are explored, the 1-hr-resolution multispacecraft OMNI2 solar wind data set (King & Papitashvili, 2005) for the years 1963–2013 is used. The OMNI2 data set is available at https://omniweb.gsfc.nasa.gov.

## 3. Plasma Properties Relevant for Turbulence Studies

Using the 1-hr-resolution OMNI2 data set, six plasma properties are binned and the occurrence distributions of those properties for the four types of solar wind plasma are plotted in Figure 2. Figure 2a displays the solar wind speed $v_{sw}$ at 1 AU. What is taken as "fast solar wind" is usually coronal-hole-origin plasma (red); however, ejecta can also be fast, as can be streamer belt-origin plasma, particularly if that plasma is pushed radially outward by coronal-hole-origin plasma. "Slow solar wind" is often taken to be plasma with

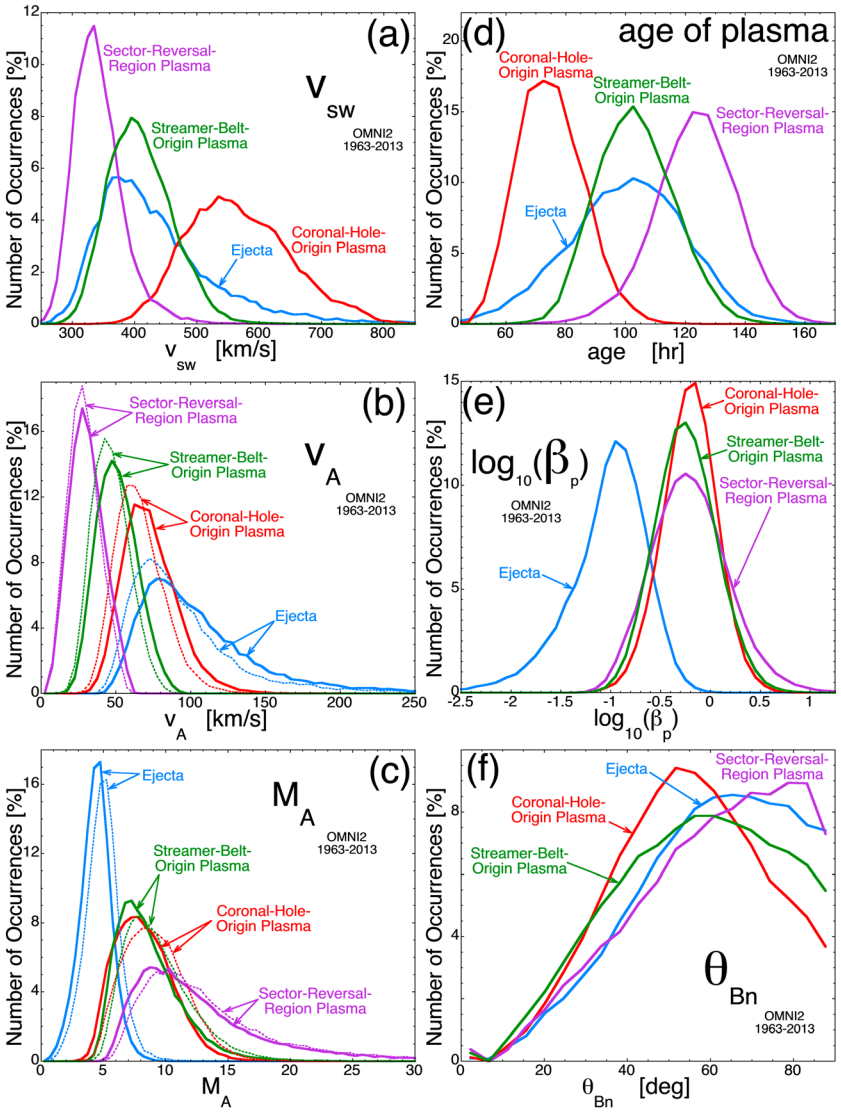


**Figure 2.** Using the 1963–2017 OMNI2 data set, the occurrence distributions of six plasma properties are binned for the four different types of solar wind plasma: (a) the speed of the solar wind, (b) the Alfvén speed in the solar wind plasma, (c) the Alfvén Mach number of the solar wind, (d) the age of the plasma at 1 AU, (e) the logarithm of the proton beta of the plasma, and (f) the angle between the 1-hr-average magnetic field vector and the radial direction.

$v_{sw} \leq 450$ km/s (e.g., Bruno et al., 2003; Carbone et al., 2004; Hadid et al., 2017; Roberts et al., 2017; Teodorescu et al., 2015): Figure 2a shows that this $v_{sw} \leq 450$ km/s plasma can be streamer-belt-origin plasma, ejecta, and sector-reversal-region plasma. Sector-reversal-region plasma can also be called "the very slow solar wind", although above 300 km/s the wind can also be ejecta or streamer-belt-origin plasma.

Figure 2b displays the occurrence distribution of Alfvén speed values $v_A$ in the four types of plasma. The thick solid curves are for the Alfvén speed $v_A = B_{mag}/(4\pi m_p n_p)^{1/2}$ based on the protons, and the thin dashed curves are for the Alfvén speed including the mass density of the alpha particles in the solar wind. The plasma and magnetic field data in the OMNI2 data set are obtained from different spacecraft over the years 1963–2013; OMNI2 does not use the alpha measurements from ACE. For the dashed curves in Figure 2b the Alfvén speed is not calculated when the alpha density is not available in the OMNI2 data set. Statistically in the OMNI2 data set, correcting the Alfvén speed with the alpha number density reduces the proton Alfvén speed by 6.6 ± 3.7%. As shown in Figure 2b, ejecta (often with a strong magnetic field) tends to have the highest values of $v_A$. Sector-reversal-region plasma tends to have the lowest values of $v_A$. In Figure 2c the Alfvén

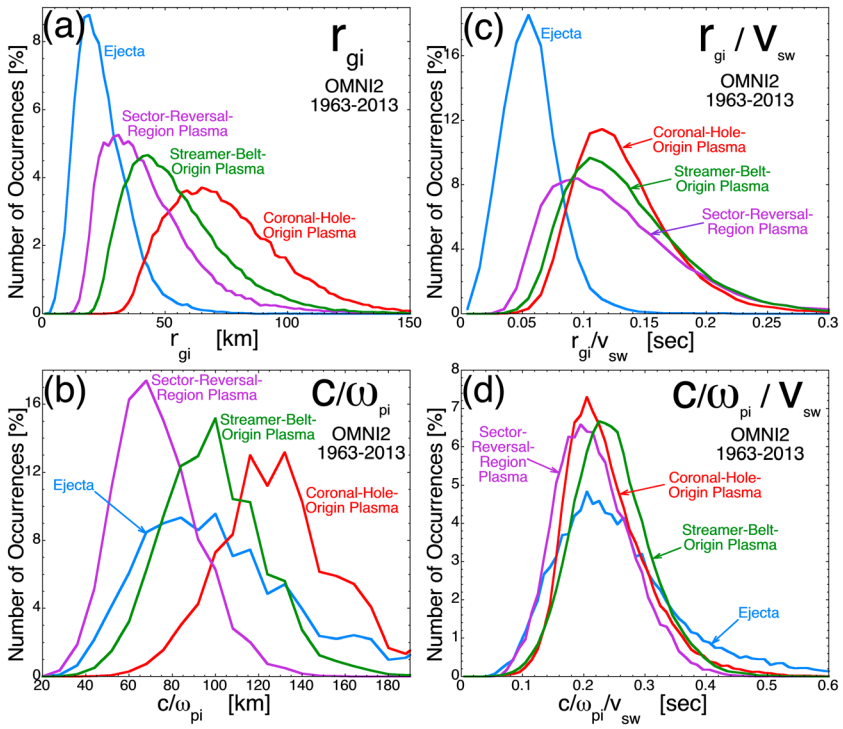


**Figure 3.** For the 1963–2017 OMNI2 data set the plasma scale sizes (a) $r_{gi}$ and (b) $c/\omega_{pi}$ are binned for the four types of plasma along with the advection timescales (c) $r_{gi}/v_{sw}$ and (d) $(c/\omega_{pi})/v_{sw}$.

Mach number $M_A = v_{sw}/v_A$ (based on the proton Alfvén speed) of the solar wind is binned as the thick solid curves and the Mach number based on the alpha particle-corrected Alfvén speed (where it is available in the OMNI2 data set) is binned as the thin dashed curves; as was the case in Figure 2b, correcting the Alfvén speed results in a noticeable but not overwhelming difference. $M_A$ is important for considerations of the validity of Taylor's approximation to convert time series turbulence measurements into wave number measurements. It is well known that ejecta tends to have lower Mach numbers (e.g., Gosling et al., 1987; Lavraud & Borovsky, 2008). Even though sector-reversal-region plasma tends to have the lowest values of $v_{sw}$ (cf. Figure 2a), it has the highest values of $M_A$.

In Figure 2d the temporal age of the solar wind plasma at 1 AU (the time since the plasma left the corona) is binned for the four plasma types, with the age being approximated by (1 AU)/$v_{sw}$, with the caveat that the speed of a parcel of solar wind often varies between the Sun and 1 AU. Sector-reversal-region plasma tends to be twice as old as coronal-hole-origin plasma. The logarithm of the proton beta $\beta_p = 8\pi n_p k_B T_p/B_{mag}{}^2$ is binned in Figure 2e. The well-known low beta values of ejecta (e.g., Gosling et al., 1987; Lepping et al., 2005) are clear in Figure 2e, with the other three types of plasma having typical proton beta values of $\beta_p \sim 1$. Figure 2f plots the occurrence distribution of the hourly averaged values of $\theta_{Bn} = \text{Arccos}(|B_r|/B_{mag})$. For conversion of time series into spatial series, $\theta_{Bn}$ is approximately the angle between the solar wind flow vector and the magnetic field direction. The magnetic field in coronal-hole-origin plasma and streamer-belt-origin plasma tends to have Parker-spiral field orientations (Xu & Borovsky, 2015) with fluctuations about the Parker spiral direction: in Figure 2f $\theta_{Bn}$ tends to be larger for streamer-belt-origin plasma (green curve) than for coronal-hole-origin plasma (red curve), because it has lower values of $v_{sw}$ than does coronal-hole-origin plasma. Ejecta and sector-reversal-region plasma tend not to have Parker spiral-oriented magnetic fields (Borovsky, 2010a; Xu & Borovsky, 2015); those plasmas tend to have magnetic-field orientations that are perpendicular to the radial direction (cf. Figure 3 of Borovsky, 2010a, specifically for ejecta). In Figure 2f the tendency to have $\theta_{Bn}$ near 90° is seen for those two plasma types (blue and purple curves).

In Figure 3 the proton gyroradius $r_{gi} = (k_B T_p/m_p)^{1/2}/(eB_{mag}/m_p c)$ and ion inertial length (ion skin depth) $c/\omega_{pi} = c/(4\pi n_p e^2/m_p)^{1/2}$ are explored. For the physics of turbulence and the physics of solar wind structure,

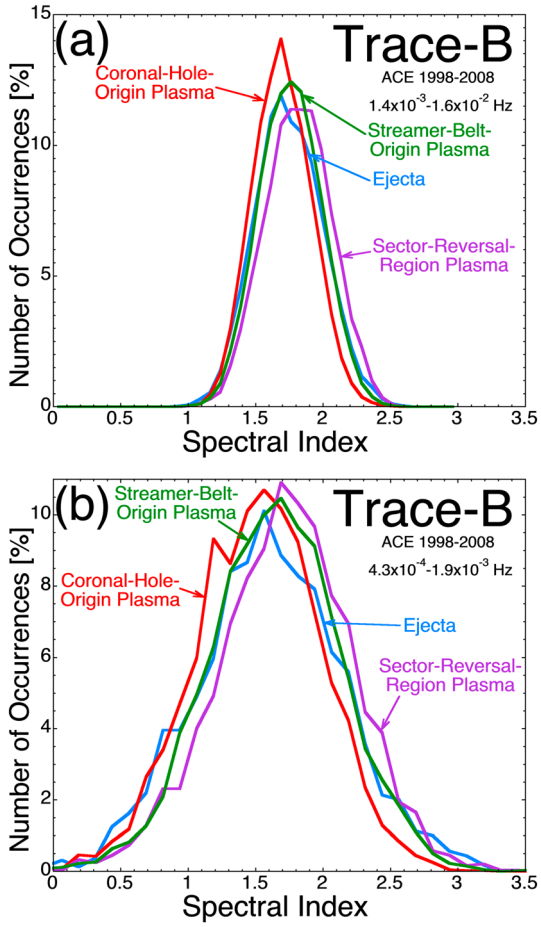


**Figure 4.** The trace-B spectral index of the solar wind is binned for the four types of solar wind plasma, (a) at higher frequencies and (b) at lower frequencies.

both of these parameters are of interest for their physical connection to the high-frequency breakpoint of the Fourier spectrum, either through the onset of kinetic plasma wave damping (e.g., Bruno & Trenchi, 2014; D'Amici et al., 2019; Gary, 1999; Gary & Borovsky, 2004, 2008; Howes et al., 2008; Leamon et al., 1998, 1999; Podesta, 2012; Podesta et al., 2010), the onset of dispersion of plasma waves (Sahraoui et al., 2010, 2012; Saito et al., 2010; Stawicki et al., 2001; TenBarge et al., 2012), or via limitations on the thicknesses of current sheets and ion velocity shears (e.g., Borovsky & Podesta, 2015; Podesta & Borovsky, 2016). Figure 3a reveals a statistical separation in the values of $r_{gi}$ between the four plasma types, with the values of $r_{gi}$ tending to increase from (1) ejecta to (2) sector-reversal-region plasma to (3) streamer-belt-origin plasma to (4) coronal-hole-origin plasma. Figure 3b shows a clear progression of the size of $c/\omega_{pi}$ from (1) sector-reversal-region plasma to (2) streamer-belt-origin plasma, to (3) coronal-hole-origin plasma, with ejecta having a broader range of $c/\omega_{pi}$ values. The timescales associated with the spatial scales $r_{gi}$ and $c/\omega_{pi}$ being swept past a spacecraft at $v_{sw}$ are calculated and binned for the four types of plasma in Figures 3c and 3d. (The actual timescales will also have a slant-angle, ~$\theta_{Bn}$, dependence that varies with the orientation of the gradient with respect to the solar wind velocity vector.) Whereas the values of $r_{gi}$ and $c/\omega_{pi}$ in Figures 3a and 3b tended to be well separated in the various types of plasmas, the timescales $r_{gi}/v_{sw}$ and $(c/\omega_{pi})/v_{sw}$ are less well separated in Figures 3c and 3d. The only strong separation (Figure 3c) is that the timescale $r_{gi}/v_{sw}$ in ejecta (blue curve) is significantly lower than the timescale $r_{gi}/v_{sw}$ in the three other types of plasma.

## 4. Spectral Indices of Solar Wind Magnetic and Velocity Fluctuations

The power spectral density is fit by a spectral index "i" in log (power)-log (frequency) space over a limited frequency range, which is a fit to the power spectral density of the form $f^{-i}$; assuming the Taylor frozen-in approximation $f = v_{sw}k$ holds, the index $i$ is a fit to the power spectral density of spatial fluctuations in the plasma of the form $k^{-i}$.

In Figure 4 the trace-B spectral index of the solar wind is binned for the four types of plasma. The top panel utilizes 1-hr intervals of 3-s ACE magnetic field data with the spectral index fitted from a structure function and the bottom panels utilize 4.5-hr intervals of 64-s ACE magnetic field data (in the ACE merged plasma and magnetic field data set) with the spectral index fitted from a periodogram. The spectral indices are fit over the frequency range $1.4 \times 10^{-3}$ to $1.6 \times 10^{-2}$ Hz (period range 64 s to 12 min) in the top panel and fit over the frequency range $4.3 \times 10^{-4}$ to $1.9 \times 10^{-3}$ Hz (period range 8.8–38.8 min) in the bottom panel. Note that there is a significant spread in the values obtained for the spectral index from data interval to data interval (see also Figure 3 of Tessein et al. (2009), Figure 10a of Tessein et al. (2011), or Figure 5 of Borovsky (2012a)): because of statistics, the spread in values obtained with the 64-s data in the lower frequency range (Figure 4b) is greater than the spread obtained with the 3-s data in the higher frequency range (Figure 4a). At both higher frequencies (Figure 4a) and lower frequencies (Figure 4b) the trace-B spectral index has similar statistics in the four types of plasma, with the trace-B spectral slope slightly shallower for coronal-hole-origin plasma (red) in both frequency ranges and the trace-B spectral index slightly steeper for sector-reversal-region plasma (purple). The trace-B spectral index being slightly shallower in coronal-hole-origin plasma is in agreement with the analysis in Table 5 of Borovsky (2012) using the Zhao et al. (2009) categorization scheme (see Table 5 of Borovsky, 2012). This is also seen in Figure 14 of Borovsky and Denton (2010) where the mean value of the magnetic spectral index becomes more shallow in crossing corotating-interaction-region stream interfaces into coronal-hole-origin plasma.

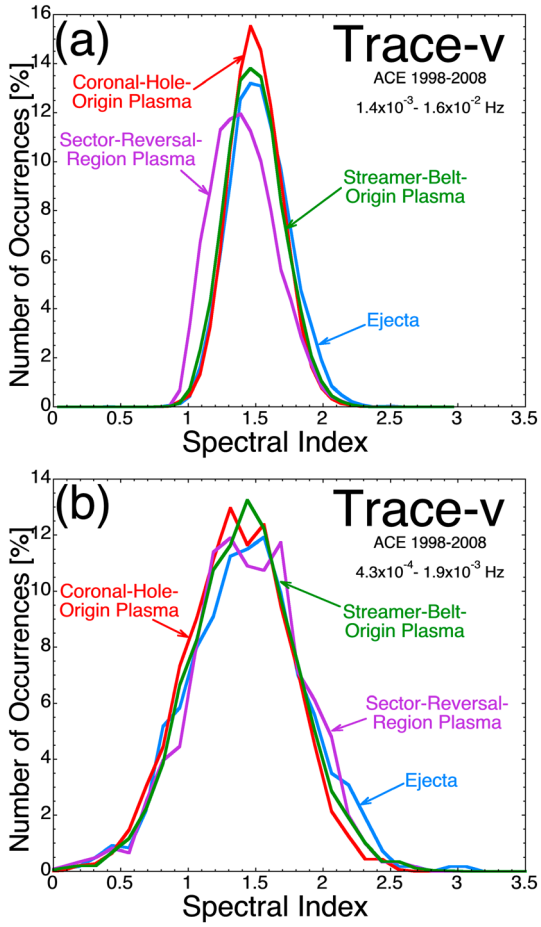


**Figure 5.** The trace-v spectral index of the solar wind is binned for the four types of solar wind plasma, (a) at higher frequencies and (b) at lower frequencies.

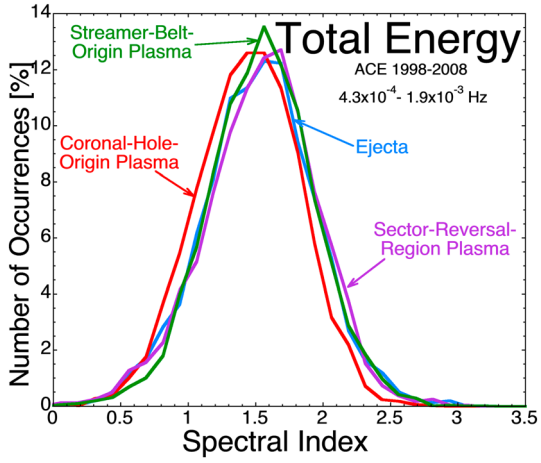


**Figure 6.** The total energy spectral index of the solar wind is binned for the four types of solar wind plasma at lower frequencies.

In Figure 5 the trace-v spectral indices are binned for the four types of plasma, with the 64-s to 12-min structure-function analysis in Figure 5a and the 8.8- to 38.8-min periodogram analysis in Figure 5b. As is well known (Boldyrev et al., 2011; Borovsky, 2012a; Chen et al., 2013; Podesta, 2011; Podesta et al., 2007; Salem et al., 2009; Tessein et al., 2009), the trace-v spectral indices (Figure 5) are shallower than the trace-B spectral indices (Figure 4). The lower-frequency analysis in Figure 5b shows similar statistics for the trace-v spectral index in all four types of plasma; the similarity of the trace-v spectral indices in different types of plasma is in agreement with the analysis in Table 5 of Borovsky (2012) using the Zhao et al. (2009) categorization scheme. The higher-frequency analysis in Figure 5a indicates a statistically shallower trace-v spectral index for sector-reversal-region plasma (purple). Comparing the red curves in Figures 4 and 5, it is the case that in coronal-hole-origin plasma the spectral indices of $v$ and $B$ are the closest to each other (see also the right-hand side of Figure 14 of Borovsky and Denton (2010)).

In Figure 6 the spectral index of the total energy fluctuations $\delta E = m_p n_p \delta v^2/2 + \delta B^2/8\pi$ is binned for the four plasma types in the lower frequency range. The plot indicates that there is not much statistical difference between the spectral indices of $E$ in the four types of plasma, but the spectral index in coronal-hole-origin plasma (red) may be slightly shallower than that in the other types of plasma. The total-energy spectral index being slightly shallower in coronal-hole-origin plasma is in agreement with the analysis of Borovsky (2012) using the Zhao et al. (2009) categorization scheme.

In Figures 7a and 7b the spectral indices of the outward $Z^{out}$ and inward $Z^{in}$ Elsässer variables (cf. Tu et al., 1989; Vasquez et al., 2018) are binned for the four types of plasma, following the inward-outward convention of Tu and Marsch (1995). Note that only the proton mass density is used in normalizing the magnetic field vector in calculating the Elsässer variables. The analysis is for the lower-frequency 8.8- to 38.8-min range. In both panels it is evident that the $Z^{out}$ and $Z^{in}$ spectral indices are both lower in coronal-hole-origin plasma (red curves), particularly the inward $Z^{in}$ spectral index. The $Z^{out}$ and $Z^{in}$ spectral indices being shallower in coronal-hole-origin plasma (particularly the $Z^{in}$ index) is in agreement with the analysis in Table 5 of Borovsky (2012) using the Zhao et al. (2009) categorization scheme. This finding is also consistent with the observations in Figure 16a of Borovsky and Denton (2010) where the inward and outward spectral indices tend to weaken in crossing from slow solar wind (mostly streamer-belt-origin plasma) to fast solar wind (coronal-hole-origin plasma) across corotating-interaction-region stream interfaces, with the weakening of the inward indices being greatest. The pattern of spectral indices in Figure 7 is consistent with the pattern in lines 3 and 6 of Table 1b of Marsch and Tu (1990a) containing Helios measurements at ~0.9 AU: they find the "high-frequency" $Z^{out}$ ($e^+$) spectral index shallower for fast wind (line 3) and the "high-frequency" $Z^{in}$ ($e^-$) spectral index much shallower for fast wind. For highly Alfvénic solar wind at 1 AU (i.e., coronal-hole-origin plasma), Wang et al. (2018) argue that the shallow $Z^{in}$ spectrum is owed to the presence of noise in the solar wind $Z^{in}$ measurements. The results in Figure 7 also agree with the patterns of Elsässer spectral slopes recorded in Table 5 of Borovsky (2012a) where the Zhao et al. (2009) three-plasma categorization scheme was used.

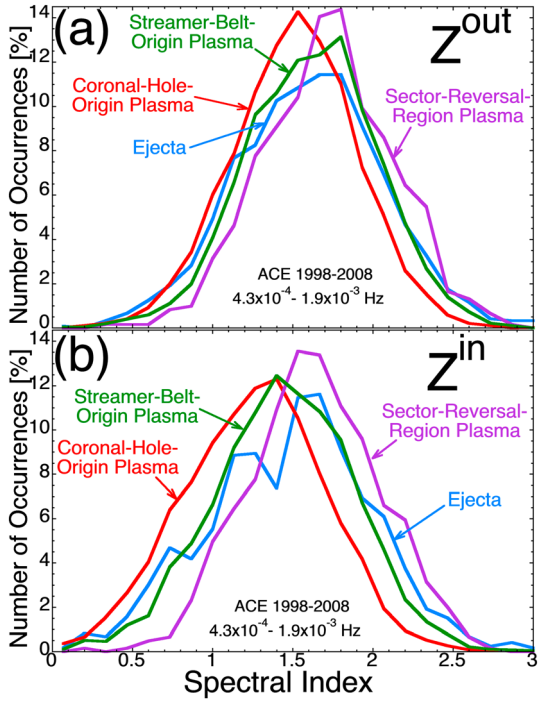


**Figure 7.** The Elsässer outward $Z^{out}$ (a) and Elsässer inward $Z^{in}$ (b) spectral indices of the solar wind are binned for the four types of solar wind plasma at lower frequencies.

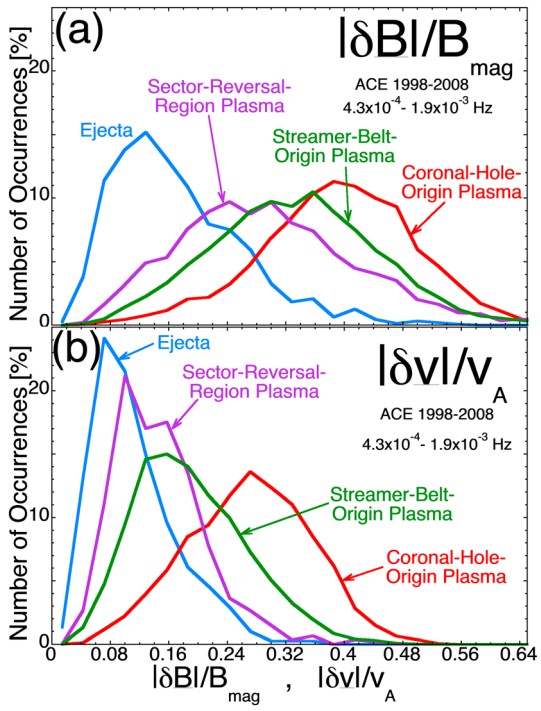


**Figure 8.** The occurrence distributions of the normalized amplitudes of the vector fluctuations (a) $|\delta \underline{B}|/B_{mag}$ and (b) $|\delta \underline{v}|/v_A$ in the frequency band $4.3 \times 10^{-4}$ to $1.9 \times 10^{-3}$ Hz for the four types of solar wind plasma are calculated using 64-s ACE data. The amplitudes are root-mean-square values of the Fourier-filtered 4.5-hr-long time series.

## 5. Fluctuation Amplitudes for Solar Wind Velocity and Magnetic Field

In Figures 8a and 8b the rms amplitudes $|\delta \underline{B}|$of the vector magnetic field fluctuations (normalized to the total magnetic field strength $B_{mag}$ in the plasma) and the rms amplitudes $|\delta v|$ of the vector velocity fluctuations (normalized to the proton Alfvén speed $v_A = B_{mag}/(4\pi m_p n_p)^{1/2}$ in the plasma) in the Fourier-filtered frequency band $4.3 \times 10^{-4}$ to $1.9 \times 10^{-3}$ Hz are binned for the four types of plasma. In both panels it is seen that the normalized amplitudes of the fluctuations are highest in coronal-hole-origin plasma (red), with the amplitudes in streamer-belt-origin plasma (green) being second highest statistically, the amplitudes being third highest in sector-reversal-region plasma (purple), and the normalized amplitudes being lowest in ejecta (blue). Note for all four types of plasma that the normalized velocity fluctuations $|\delta \underline{v}|/v_A$ (Figure 8b) are of lower amplitudes than the normalized magnetic field fluctuations $|\delta \underline{B}|/B_{mag}$ (Figure 8a; see also Figure 11d of Borovsky and Denton (2010) and Figure 15a of Borovsky, 2012a). Correcting $v_A$ for the alpha particle number density would lower $v_A$ and result in values of $|\delta \underline{v}|/v_A$ that are in the vicinity of 10% larger than those plotted: this would make the values of $|\delta \underline{v}|/v_A$ closer to but still less than the values of $|\delta \underline{B}|/B$. The fluctuation amplitudes $|\delta \underline{B}|/B_{mag}$ and $|\delta \underline{v}|/v_A$ being highest in coronal-hole-origin plasma is in agreement with the analysis in Table 5 of Borovsky (2012) using the Zhao et al. (2009) categorization scheme; however, the present analysis finds the amplitudes $|\delta B|/B_{mag}$ and $|\delta \underline{v}|/v_A$ being lowest in ejecta whereas the Borovsky (2012) analysis finds the amplitudes lowest in "noncoronal-hole-origin" plasma, which is not ejecta.

In Figure 9 the rms amplitudes of the Elsässer outward $Z^{out}$ and inward $Z^{in}$ fluctuations in the Fourier-filtered frequency band $4.3 \times 10^{-4}$ to $1.9 \times 10^{-3}$ Hz are binned for the four types of plasma. Note again that only the proton mass density is used in normalizing the magnetic field vector in calculating the Elsässer variables; if the alpha mass density were included it would reduce the magnitude of the magnetic vector relative to the velocity vector in the Elsässer vector. For purely outward traveling Alfvénic fluctuations this correction would lower the outward Elsässer amplitude by a few percent and would reduce the inward amplitude. Note for coronal-hole-origin plasma (red curves) that the outward fluctuation amplitude (Figure 9a) is much larger than the inward fluctuation amplitude (Figure 9b); the mean value of the amplitude is 2.1 times larger for $Z^{out}$ than it is for $Z^{in}$. For streamer-belt-origin plasma the outward Elsässer amplitude is also larger than the inward Elsässer amplitude; the mean value of the amplitude is 1.5 times larger for $Z^{out}$ than it is for $Z^{in}$. For ejecta and for sector-reversal-region plasma, the inward and outward Elsässer amplitudes are statistically similar.

## 6. The Populations of Current Sheets and Velocity Shears

Strong current sheets (directional discontinuities) are of interest because they carry the majority of the inertial range Fourier power of the magnetic power spectral density of the solar wind (Borovsky, 2010b; Siscoe et al., 1968); it is likely that strong velocity shears (vorticity layers) similarly dominate the Fourier power of the velocity power spectral density. To examine the occurrence statistics of strong current sheets (i.e., strong

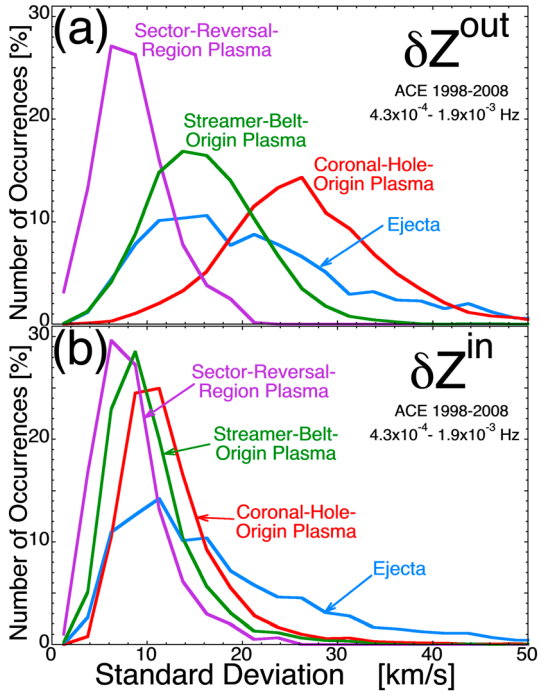


**Figure 9.** The occurrence distributions of the normalized amplitudes of (a) $Z^{out}$ and (b) $Z^{in}$ in the frequency band $4.3 \times 10^{-4}$ to $1.9 \times 10^{-3}$ Hz for the four types of solar wind plasma are calculated using 64-s ACE data. The amplitudes are root-mean-square values of the Fourier-filtered 4.5-hr-long time series.

sudden rotations of the magnetic field vector) and strong sudden velocity shear layers (vorticity layers) in the different types of solar wind plasma, the 128-s changes in the magnetic field vector (Borovsky, 2008) and in the velocity vector (Borovsky, 2012b) are examined, respectively. Using ACE 64-s magnetic field measurements in the years 1998–2007 the quantity $|\delta\underline{B}|/B = |\underline{B}(t + 64\text{ s}) - \underline{B}(t - 64\text{ s})|/B_{mag}(t)$ is binned separately for the four types of plasma, and the occurrence distributions are plotted in Figure 10 as the thick curves. In the same years 64-s ACE plasma measurements are used to bin the quantity $|\delta\underline{v}|/v_A = |\underline{v}(t + 64\text{ s}) - \underline{v}(t - 64\text{ s})|/v_A(t)$, and the occurrence distributions for the four types of plasma are plotted in Figure 10 as the thin curves. The binning in the thin curves uses the proton number density to calculate $v_A$: correcting this for the alpha particle number density would lower $v_A$ and result in values of $|\delta\underline{v}|/v_A$ that are in the vicinity of 10% larger than those plotted. This would make the values of $|\delta\underline{v}|/v_A$ closer to but still less than the values of $|\delta\underline{B}|/B$. Strong current sheets appear as the larger values of $|\delta\underline{B}|/B$ and strong velocity shear layers appear as larger values of $|\delta\underline{v}|/v_A$. Figure 10 shows that for each of the four types of plasma, strong current sheets $|\delta\underline{B}|/B$ are more prevalent (i.e., stronger) than strong velocity shear layers $|\delta\underline{v}|/v_A$. For both strong current sheets and strong velocity shear layers, coronal-hole-origin plasma (red) has the highest prevalence, followed by streamer-belt-origin plasma (green), then sector-reversal-region plasma (purple), with ejecta (blue) having the weakest occurrence rate of strong current sheets and strong velocity shear layers. The occurrence rate of strong current sheets being highest in coronal-hole-origin plasma and lowest in ejecta is in agreement with the analysis of Borovsky (2012) using the Zhao et al. (2009) categorization scheme (see the $N_d$ number in Table 5 of Borovsky, 2012).

## 7. The Alfvénicity of the Solar Wind Fluctuations

In Figure 11a the ratio $\delta Z^{out}/\delta Z^{in}$ of the rms amplitudes of the $\underline{Z}^{out}$ to $\underline{Z}^{in}$ fluctuations in the frequency band $4.3 \times 10^{-4}$ to $1.9 \times 10^{-3}$ Hz are binned for the four types of solar wind plasma. The outward-to-inward imbalance is greatest in coronal-hole-origin plasma (red), second largest in streamer-belt-origin plasma (green), and similarly on the order of unity in ejecta (blue) and sector-reversal-region plasma (purple), with the imbalance being lowest in sector-reversal-region plasma. The dominance of the outward-to-inward imbalance in coronal-hole-origin plasma is also reflected in the right-hand side of Figure 16 of Borovsky and Denton (2010) after ACE crosses leading-edge (corotating-interaction-region) stream interfaces into coronal-hole-origin plasma and in the left-hand side of Figure 15 of Borovsky and Denton (2016) before ACE crosses trailingedge stream interfaces out of coronal-hole-origin plasma. The ratio $\delta Z^{out}/\delta Z^{in}$ being highest in coronal-hole-origin plasma is in agreement with the analysis in Table 5 of Borovsky (2012) using the Zhao et al. (2009) categorization scheme. In the present study the ratio is found to be lowest in sector-reversal-region plasma, a category that the Zhao et al. (2009) scheme does not have; the Borovsky (2012) analysis found the ratio to be lowest in ejecta with the ratio slightly higher in "noncoronal-hole-origin" plasma.

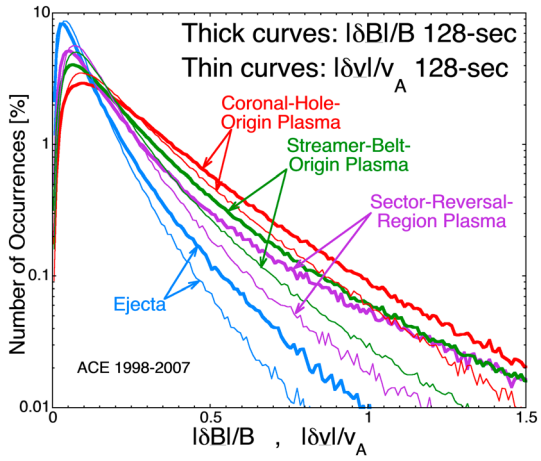


**Figure 10.** The 128-s changes in the vector $B$ (normalized to $B_{mag}$) and the 128-s change in the vector $v$ (normalized to $v_A$) are binned for the four types of solar wind plasma using 64-s ACE measurements in the years 1998–2007. Large values of $|\delta\underline{B}|/B_{mag}$ represent crossings of strong current sheets and large values of $|\delta\underline{v}|/v_A$ represent crossings of strong velocity shears.

In Figure 11b the Alfvénicity $|A|$ of the fluctuations at 128 s is binned, where $|A| = |\Delta\underline{v} \cdot \Delta\underline{B}/|\Delta\underline{v}||\Delta\underline{B}|$ with $\Delta\underline{v}(t) = \underline{v}(t + 64\text{ s}) - \underline{v}(t - 64\text{ s})$ and $\Delta\underline{B}(t) = \underline{B}(t + 64\text{ s}) - \underline{B}(t - 64\text{ s})$. Events with $|A| \approx 1$ are highly correlated and a distribution of uncorrelated events would appear as the black dashed line in Figure 11b. The high degree of correlation between the

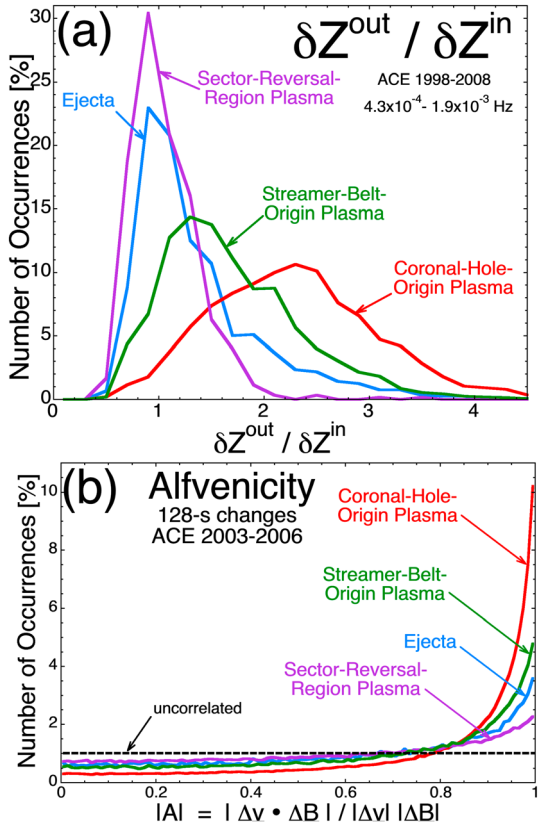


**Figure 11.** (a) The ratio of the amplitudes of $Z^{out}$ and $Z^{in}$ in the frequency band $4.3 \times 10^{-4}$ to $1.9 \times 10^{-3}$ Hz is binned for the four types of solar wind plasma. The amplitudes are root-mean-square values of the Fourier-filtered 4.5-hr-long time series. (b) The Alfvénicity of 128-s changes in the vectors $\underline{v}$ and $\underline{B}$ in the 64-s ACE data set is binned for the four types of plasma.

changes $\Delta\underline{v}$ and $\Delta\underline{B}$ in coronal-hole-origin plasma (red curve) are seen, with the correlations being second highest in streamer-belt-origin plasma, and third highest in ejecta. The correlations are lowest in sector-reversal-region plasma (purple curve), even lower than in ejecta (blue).

Note the differences in the Alfvénicity between the Alfvénic stream-belt-origin plasma and the non-Alfvénic sector-reversal-region plasma, both of which are "slow winds." This Alfvénic versus non-Alfvénic slow wind has been pointed out before (D'Amicis & Bruno, 2015; D'Amici et al., 2016, 2019). D'Amici et al. (2019) argued that the non-Alfvénic slow wind originates from streamers and that the Alfvénic slow wind originates from the edges of coronal holes; the present study is in agreement with these conclusions, with the caveat that it is controversial whether streamer-belt-origin plasma comes from coronal-hole edges (Arge et al., 2003; Wang & Sheeley, 1990), from canopy reconnection of streamer-belt magnetic loops (Fisk et al., 1999; Subramanian et al., 2010), or from *S*-web lanes of open flux in the streamer belt (Antiochos et al., 2011; Crooker et al., 2012).

## 8. Spectral Indices in Belcher and Davis Magnetic Coordinates

In the Belcher and Davis (1971) (*X*,*Y*,*Z*) coordinate system the spectral indices of $B_x$, $B_y$, $B_z$, $v_x$, $v_y$, and $v_z$ are calculated in the higher-frequency range $1.4 \times 10^{-3}$ to $1.6 \times 10^{-2}$ Hz. The *X*, *Y*, and *Z* directions are calculated relative to the mean magnetic-field direction for 1-hr intervals of the ACE data set. The $\underline{Z}$ direction is the direction of the mean magnetic field, *X* is in the $Z \times r$ direction ($\underline{r}$ radially outward from the Sun), and *Y* is in the $\underline{Z} \times \underline{X}$ direction.

The occurrence distributions of the spectral indices are plotted in Figure 12 with the magnetic indices to the left and the velocity spectral to the right. Figures 12a and 12b show that in the *X* and *Y* directions the magnetic spectral index is statistically similar in those two directions for all four types of plasma, with the spectral index of coronal-hole-origin plasma (red) slightly shallower and the spectral index of sector-reversal-region plasma (purple) slightly steeper. In the *Z* direction (Figure 12c) the magnetic spectral index statistically varies with the type of plasma, with the spectral index being definitely steepest in sector-reversal-region plasma (purple) and definitely shallowest in coronal-hole-origin plasma (red). It is clearly the case that the magnetic spectral index in coronal-hole-origin plasma is shallower in the *Z* direction than it is in the *X* and *Y* directions.

The pattern of velocity spectral indices is different. In all three directions (Figures 12d–12f) the spectral index of sector-reversal-region plasma (purple curves) is shallower than the indices for the other three plasmas. (See also Figure 5a.) Unlike the case of the magnetic spectral indices where the pattern in the *Z* direction differed from the patterns in the *X* and *Y* directions, for the velocity spectral index the patterns are similar in all three directions.

## 9. Anisotropy of Magnetic and Velocity Fluctuations

In Figure 13 the anisotropy of the magnetic-field fluctuations (Figure 13a) and velocity fluctuations (Figure 13b) measured using 1-hr intervals of ACE measurements in the years 1998–2008 are plotted. The anisotropy is measured with respect to the direction of the 1-hr mean magnetic field vector $B_{mean}$ in the solar wind.

The magnetic fluctuation anisotropy is $(\delta B_\perp)^2/(\delta B_{||})^2$, where $\delta B_\perp$ is the rms amplitude of magnetic field fluctuations in the 3-s measurements of $\underline{B}$ in the directions perpendicular to $B_{mean}$ and $\delta B_{||}$is the rms amplitude of 3-s measurements of the component of *B* that is parallel to $B_{mean}$. The magnetic fluctuation anisotropy in

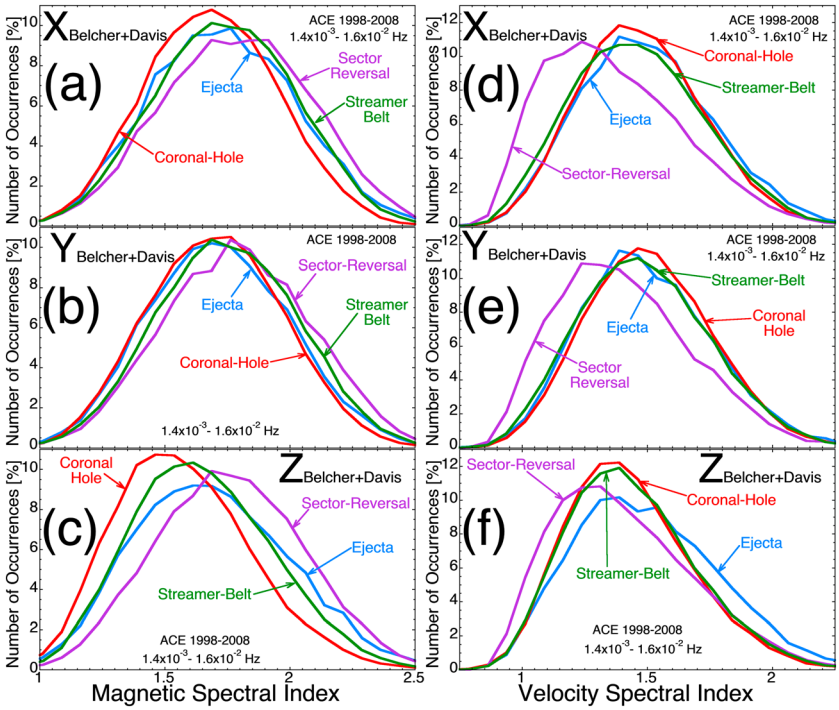


**Figure 12.** In the Belcher and Davis magnetic coordinate system the component magnetic spectral indices (a)–(c) and the component velocity spectral indices (d)–(f) are binned for the four types of solar wind plasma.

Figure 13a tends to be greater than unity for all four types of plasma. The largest values of the anisotropy $(\delta B_\perp)^2/(\delta B_{||})^2$ occur in ejecta (blue), and the values of $(\delta B_\perp)^2/(\delta B_{||})^2$ are statistically lowest in sector-reversal-region plasma (purple). The larger values of $(\delta B_\perp)^2/(\delta B_{||})^2$ occurring in ejecta is consistent with Figure 2 of Smith et al. (2006) where larger values of $(\delta B_\perp)^2/(\delta B_{||})^2$ were found for magnetic clouds.

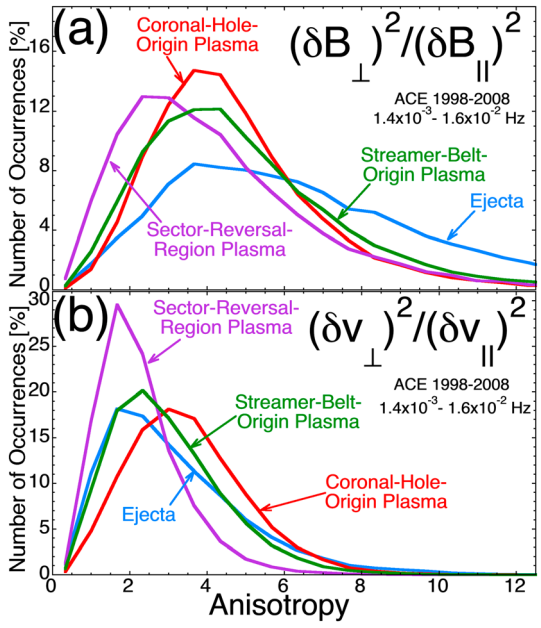


**Figure 13.** The anisotropy of vector magnetic fluctuations (a) and the anisotropy of vector velocity fluctuations (b) are binned for the four types of plasma. The amplitudes are root-mean-square values of the 1-hr-long time series.

The velocity fluctuation anisotropy is $(\delta v_\perp)^2/(\delta v_{||})^2$, where $\delta v_\perp$ is the rms amplitude of vector velocity fluctuations in the 64-s measurements of $v$ in the directions perpendicular to $B_{\text{mean}}$ and $\delta v_{||}$is the rms amplitude of 64-s measurements of the component of $v$ that is parallel to $\underline{B}_{\text{mean}}$. In all four plasmas the values of $(\delta v_\perp)^2/(\delta v_{||})^2$ tend to be greater than unity, with the values statistically largest in coronal-hole-origin plasma (red) and smallest in sector-reversal-region plasma (purple).

Comparing Figures 13a and 13b it is seen that the magnetic fluctuation anisotropy $(\delta B_\perp)^2/(\delta B_{||})^2$ is on average larger than the velocity fluctuation anisotropy $(\delta v_\perp)^2/(\delta v_{||})^2$. (See also Figures 1 and 4 of Bruno et al. (1999)).

Note that even if $\delta\underline{B}$ is strictly perpendicular to the local direction of the magnetic field $B$, the wiggle of the direction of $B$ will project some of the $\delta B_\perp$ fluctuations in the direction parallel to an averaged $<B> = B_{\text{mean}}$. Under these circumstances one would expect to see the ratio $\delta B_{||}/\delta B_\perp$ increase as the normalized magnitude of the fluctuations $|\delta\underline{B}|/B_{\text{mag}}$ increase, with $|\delta\underline{B}|/B_{\text{mag}}$ being a "wiggle angle" of the magnetic field about its mean direction (cf. Borovsky, 2010a). In Figure 14 $\delta B_{||}/\delta B_\perp$ is plotted as a function of $|\delta\underline{B}|/B_{\text{mag}}$ in gray for all data points in the 1998–2008 "ACE Hourly Data Parameters for Magnetospheric Driving" data set, with every data point representing the analysis of 1 hr of ACE magnetic field measurements. (Note the related plots $(\delta B_\perp)^2/(\delta B_{||})^2$ versus $|\delta\underline{B}|/B_{\text{mag}}$ in Figure 4a of Smith et al. (2006) and in Figure 7 of Tessein et al. (2011).)

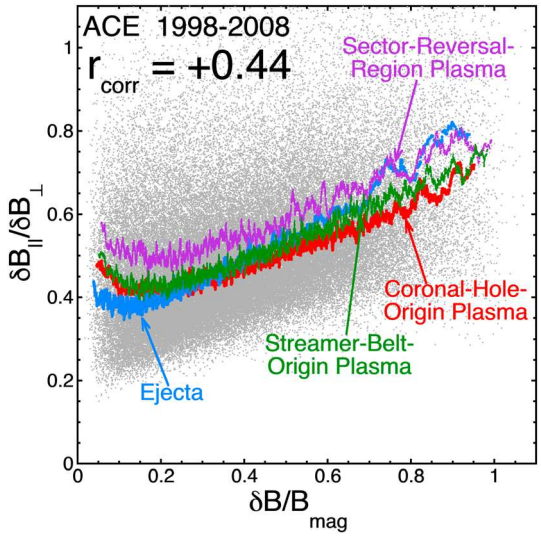


**Figure 14.** The ratio of the amplitudes of parallel-to-$B_{ave}$ magnetic fluctuations to perpendicular-to-$B_{ave}$ magnetic fluctuations is plotted as a function of $|\underline{\delta B}|/B_{mag}$ for all of the 1998–2008 ACE data set: Each gray point is 1 hr of measurement. The amplitudes are root-mean-square values of the 1-hr-long time series. The four color curves are 100-point running averages of $\delta B_{||}/dB_{\perp}$ for each of the four types of plasma.

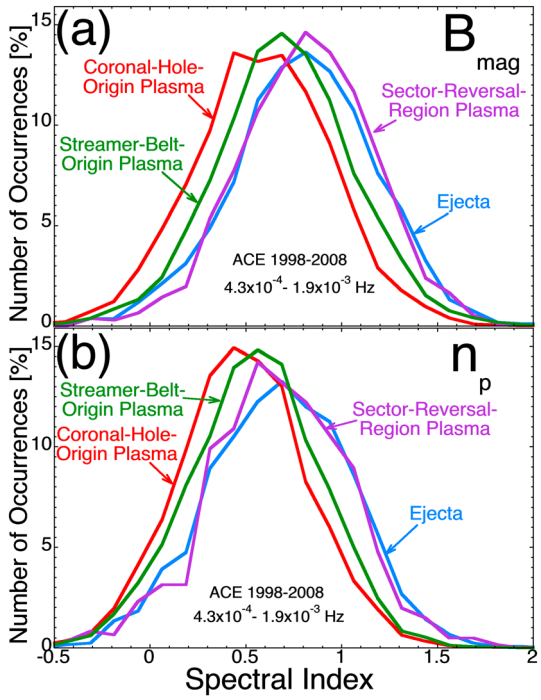


**Figure 15.** The spectral index of magnetic field strength fluctuations (a) and proton number density fluctuations (b) in the frequency range $4.3 \times 10^{-4}$ to $1.9 \times 10^{-3}$ Hz are binned for the four types of plasma using 64-s ACE measurements.

Note in Figure 14 the positive correlation between $\delta B_{||}/\delta B_{\perp}$ and $|\underline{\delta B}|/B_{mag}$ with a Pearson linear correlation coefficient (equation (11.17) of Bevington and Robinson, 1992) of $r_{corr} = +0.44$ for the gray points, where a random correlation with $N = 26{,}333$ data points would be $|r_{corr}| < 2/(N+1)^{1/2} = 0.012$ (e.g., Bendat & Piersol, 1971; Beyer, 1966). Note in Figure 14 that $\delta B_{||}/\delta B_{\perp}$ does not go to zero as $|\underline{\delta B}|/B_{mag}$ goes to zero. This may indicate that there is a population of fluctuations $\delta B_{mag}$, which gives a $\delta B_{||}$ that is not associated with the projection of $\delta B_{\perp}$ onto the parallel-to-$B_{mean}$ direction. (These $\delta B_{mag}$ fluctuations may represent compressions (e.g., Tu & Marsch, 1994), pressure balance structures (e.g., Riazantseva et al., 2005), slow mode waves (e.g., Verscharen et al., 2017), mirror mode waves (e.g., Winterhalter et al., 1994), etc.) If the total amplitude of the fluctuations $|\underline{\delta B}|$ is typically represented by $\delta B_{\perp}$, then $\delta B_{||}/\delta B_{\perp}$ should decrease with increasing $|\underline{\delta B}|/B_{mag}$ for these $B_{mag}$ fluctuations. In Figure 14 the gray points are separated into four groups according to the four types of plasma, and a 100-point running average of $\delta B_{||}/\delta B_{\perp}$ is plotted for each of the four types of plasma: the average for coronal-hole-origin plasma is plotted in red, the average for streamer-belt-origin plasma is plotted in green, the average for sector-reversal-region plasma is plotted in purple, and the average for ejecta is plotted in blue. Note that the four running averages each show a trend of $\delta B_{||}/\delta B_{\perp}$ decreasing with increasing $|\underline{\delta B}|/B_{mag}$ for low values of $|\underline{\delta B}|/B_{mag}$. Note in these running averages that the amplitude near $|\underline{\delta B}|/B_{mag} = 0$ is greatest for sector-reversal-region plasma, second greatest for streamer-belt-origin plasma and coronal-hole-origin plasma, and smallest for ejecta: this ranking will agree with examinations of $|\underline{\delta B}|/B_{mag}$ for the four types of plasma in section 10.

## 10. Fluctuations of the Proton Number Density and Magnetic Field Strength

In Figure 15a the spectral index of the total magnetic field strength (magnetic intensity) $B_{mag}$ is binned for the four plasma types in the range 8.8–38.8 min. In all four plasmas the spectral index of $B_{mag}$ is much shallower than is the trace-B (Figure 4) or trace-v (Figure 5) spectral indices: for the entire data set the mean value and standard deviation of the $B_{mag}$ spectral index is 0.72 ± 0.38. The $B_{mag}$ spectral index tends to be shallowest in coronal-hole-origin plasma (red), with streamer-belt-origin plasma being less shallow; ejecta and sector-reversal-region plasma are the steepest. Similar trends of the $B_{mag}$ spectral index are seen in the lower-right panel of Figure 5 of Marsch and Tu (1990b) in the period range 8.3–33.3 min where the $B_{mag}$ spectral index becomes more shallow at high wind speeds.

In Figure 15b the spectral index of the proton number density $n_p$ is binned for the four plasmas in the range 8.8–38.8 min. For the entire data set the mean value and standard deviation of the number density spectral index is 0.58 ± 0.36. Similar to the spectral indices of $B_{mag}$, the spectral indices of $n_p$ tends to be shallowest in coronal-hole-origin plasma (red), with streamer-belt-origin plasma (green) being less shallow; ejecta (blue) and sector-reversal-region plasma (purple) are the steepest. Similar trends of the number density spectral index are seen in the lower-right panel of Figure 4 of Marsch and Tu (1990b) in the period range 8.3–33.3 min where the index becomes more shallow at

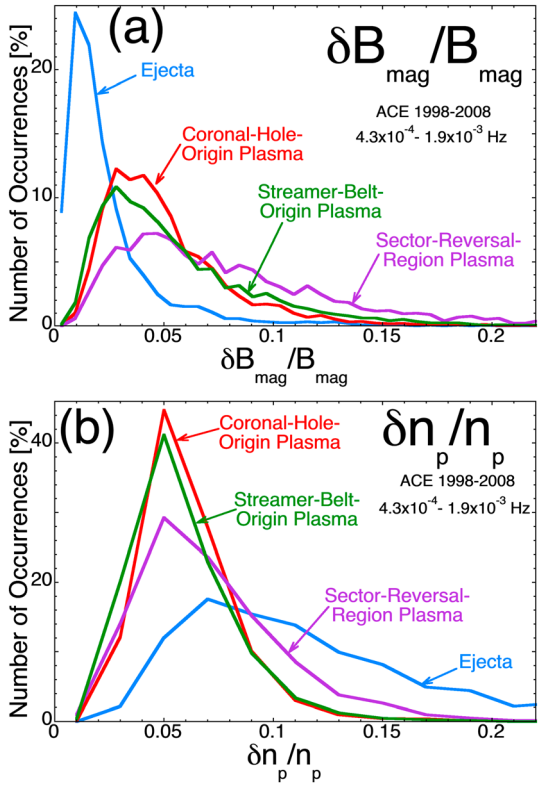


**Figure 16.** The normalized root-mean-square amplitudes of magnetic field strength fluctuations (a) and proton number density fluctuations (b) in the frequency band $4.3 \times 10^{-4}$ to $1.9 \times 10^{-3}$ Hz are binned for the four types of plasma. The amplitudes are root-mean-square values of the Fourier-filtered 4.5-hr-long time series.

high wind speeds; in a lower-frequency range (55.5–83.3 min; upper right panel of Figure 4) the number-density spectral index is invariant to wind speed.

In Figure 16a the standard deviation $\delta B_{\rm mag}$ of the temporal fluctuations of $B_{\rm mag}$ in the Fourier-filtered frequency band $4.3 \times 10^{-4}$ to $1.9 \times 10^{-3}$ Hz (normalized to the mean value of $B_{\rm mag}$) is binned for the four types of plasma. Comparing Figure 16 to Figure 8a, it is seen that the fluctuations of the field intensity $B_{\rm mag}$ are much smaller than the fluctuations of vector $B$: for the entire data set the values of $\delta B_{\rm mag}/B_{\rm mag}$ have a mean value and standard deviation of $0.056 \pm 0.040$ while $|\delta B|/B_{\rm mag}$ has $0.32 \pm 0.13$, a factor of ~5.7 lower amplitude. (The fluctuation amplitude of $B_{\rm mag}$ is clearly smaller than the fluctuation amplitude of $\underline{B}$ in Figures 5 and 6 of Goldstein et al., 1984 and in Figure 2 of Horbury et al., 2005.) In Figure 16a the amplitudes of $\delta B_{\rm mag}/B_{\rm mag}$ are clearly lowest in ejecta (blue; with ejecta often identified by low values of the magnetic field fluctuations (e.g., Burlaga et al., 1981, 1998; Cane & Richardson, 2003)). The larger values of the normalized magnetic field strength fluctuations $\delta B_{\rm mag}/B_{\rm mag}$ tend to occur in sector-reversal-region plasma (purple), which shows a "lumpy" plasma structure (Foullon et al., 2011; Viall & Vourlidas, 2015; Wang et al., 2000). These differences in the amplitudes of $|\delta \underline{B}|/B_{\rm mag}$ in the four plasma types agree with the analysis of the running averages in Figure 14 (cf. section 9).

In Figure 16b the standard deviation $\delta n$ of the temporal fluctuations of the proton number density $n_{\rm p}$ in the frequency band $4.3 \times 10^{-4}$ to $1.9 \times 10^{-3}$ Hz (normalized to the mean value of $n_{\rm p}$) is binned for the four types of plasma. The amplitudes $\delta n_{\rm p}/n_{\rm p}$ are largest in ejecta (blue), second largest in sector-reversal-region plasma (purple), and smallest (and about the same) in coronal-hole-origin plasma (red) and streamer-belt-origin plasma (green).

## 11. Summary

Using ACE solar wind measurements at 1 AU, the statistical properties of the fluctuations of $\underline{B}$, $\underline{v}$, $B_{\rm mag}$, and $n_{\rm p}$ were examined separately in four types of solar wind plasma (coronal-hole-origin plasma, streamer-belt-origin plasma, sector-reversal-region plasma, and ejecta). The findings of the analysis are summarized in Table 1. Note that the ratings (small, modest, and significant) of the sizes of the observed systematic differences are subjective.

In line 4 of Table 1 "Parker" refers to the fact that the magnetic field orientation in coronal-hole-origin plasma and in streamer-belt-origin plasma tends to be Parker spiral oriented (with noise) and "nonParker" refers to the fact that the magnetic field in sector-reversal-region plasma and in ejecta tend not to be Parker spiral oriented.

The plasma properties definitely vary between the four types of solar wind, and some of the fluctuation properties also vary between the four types. There are slight systematic variations in the trace-B, trace-v, and total energy spectral indices and stronger variations in the proton number density and magnetic field intensity spectral indices. The spectral indices of the $Z^{\rm in}$ and $Z^{\rm out}$ Elsässer fluctuations have strong systematic variations between the four plasma types. The normalized fluctuation amplitudes $|\delta \underline{B}|/B_{\rm mag}$ and $|\delta \underline{v}|/v_{\rm A}$ show strong systematic variations between the plasma types, as do the populations of strong current sheets and intense velocity shears. The perpendicular-to-parallel anisotropies of the $\underline{v}$ and $\underline{B}$ fluctuations are high in all four plasma types, with the anisotropy decreasing with increased normalized amplitudes of the fluctuations. The Alfvénicity of the $\underline{v}$ and $\underline{B}$ fluctuations varies substantially between the four plasma types, with the Alfvénicity of sector-reversal-region plasma being even weaker than the Alfvénicity of ejecta.

**Table 1**
*Summary of Findings*

| Quantity | Size of the systematic differences | Coronal hole origin plasma | Streamer belt origin plasma | Sector reversal region plasma | Ejecta | Source |
|---|---|---|---|---|---|---|
| Alfvén speed $v_A$ | significant | | | lowest | highest | Figure 2 |
| Proton beta $\beta_p$ | significant | | | | lowest | Figure 2 |
| Alfvén Mach number $M_A$ | significant | | | highest | lowest | Figure 2 |
| Field angle from radial $\theta_{Bn}$ | significant | Parker | Parker | nonParker | nonParker | Figure 2 |
| Age of plasma at 1 AU | significant | youngest | | oldest | | Figure 2 |
| Thermal proton gyroradius $r_{gi}$ | significant | largest | | | smallest | Figure 3 |
| Ion-inertial length $c/\omega_{pi}$ | significant | largest | | smallest | | Figure 3 |
| Proton gyroradius timescale $r_{gi}/v_{sw}$ | significant | | | | smallest | Figure 3 |
| Inertial-length timescale $(c/\omega_{pi})/v_{sw}$ | small | | | | | Figure 3 |
| Trace-B spectral index | small | shallowest | | | | Figure 4 |
| Trace-v spectral index | small | | | | | Figure 5 |
| Total energy spectral index | small | shallowest | | | | Figure 6 |
| $Z^{out}$ spectral index | modest | shallowest | | | | Figure 7 |
| $Z^{in}$ spectral index | modest | shallowest | | steepest | | Figure 7 |
| $B_{mag}$ spectral index | significant | lowest | | | | Figure 15 |
| $n$ spectral index | significant | lowest | | | | Figure 15 |
| Normalized amplitude $\lvert\delta\bar{B}\rvert/B_{mag}$ | significant | highest | | | lowest | Figure 8 |
| Normalized amplitude $\lvert\delta\bar{v}\rvert/v_A$ | significant | highest | | | lowest | Figure 8 |
| Normalized amplitude $\delta\bar{B}_{mag}/B_{mag}$ | significant | | | highest | lowest | Figure 16 |
| Normalized amplitude $\delta n_p/n_p$ | significant | | | | highest | Figure 16 |
| Amplitude $\delta Z^{out}$ | significant | highest | | lowest | | Figure 9 |
| Amplitude $\delta Z^{in}$ | significant | | | lowest | highest | Figure 9 |
| Prevalence of strong current sheets | significant | highest | | | lowest | Figure 10 |
| Prevalence of strong velocity shears | significant | highest | | | lowest | Figure 10 |
| Outward imbalance $\delta Z^{out}/\delta Z^{in}$ | significant | highest | | lowest | | Figure 11 |
| Alfvénicity | significant | highest | | lowest | | Figure 11 |
| Fluctuation anisotropy $(\delta B_\perp)^2/(\delta B_{\|\|})^2$ | significant | | | lowest | highest | Figure 13 |
| Fluctuation anisotropy $(\delta v_\perp)^2/(\delta v_{\|\|})^2$ | significant | highest | | lowest | | Figure 13 |
| Belcher+Davis $B_z$ spectral index | significant | shallowest | | steepest | | Figure 12 |
| Belcher+Davis $v_z$ spectral index | modest | | | shallowest | steepest | Figure 12 |

## 12. Discussion

### 12.1. Categorization by Slow Versus Fast

As seen by a spacecraft in the solar wind, the type of solar wind plasma switches in time. This study provides information that can assess the effects of "mixing apples and oranges" in the analysis of a solar wind time series. Certainly, there is a strong possibility of such mixing in time series that are multiple-hours long, and the longer the time series the higher the likelihood of mixing the properties of different plasma types from different types of regions on the solar surface. Schwenn (1983) warned about the mixing of analysis results from different types of solar wind and recommended separating the data analysis by solar wind speed $v_{sw}$: the present study suggests further separation of the data analysis into the four types of plasma. Even for the analysis of short intervals of solar wind data, it is advised to determine which type of plasma is being analyzed and to specify to which type of plasma the analysis pertains. At 1 AU this determination can be made using the simple 3D4CAT algebraic categorization scheme (equation (10) of Xu and Borovsky, 2015) if measurements of $n_p$, $v_{sw}$, $T_p$, and $B_{mag}$ are available. Other categorization schemes could also be used; other schemes might give somewhat different results.

In past studies the solar wind was often separately analyzed for "slow wind" versus "fast wind". Taking slow solar wind to be plasma with $v_{sw} \leq 450$ km/s, the 1963–2013 OMNI2 data set has slow wind being coronal-hole-origin plasma 2.5% of the time, streamer-belt-origin plasma 52.4% of the time, sector-reversal-region plasma 31.4% of the time, and ejecta 13.7% of the time; taking fast solar wind to be plasma with $v_{sw} \geq 550$ km/s the OMNI2 data set has fast wind being coronal-hole-origin plasma 88.5% of the time, streamer-belt-origin plasma 2.2% of the time, sector-reversal-region plasma 0.2% of the time, and ejecta 9.1% of the time.

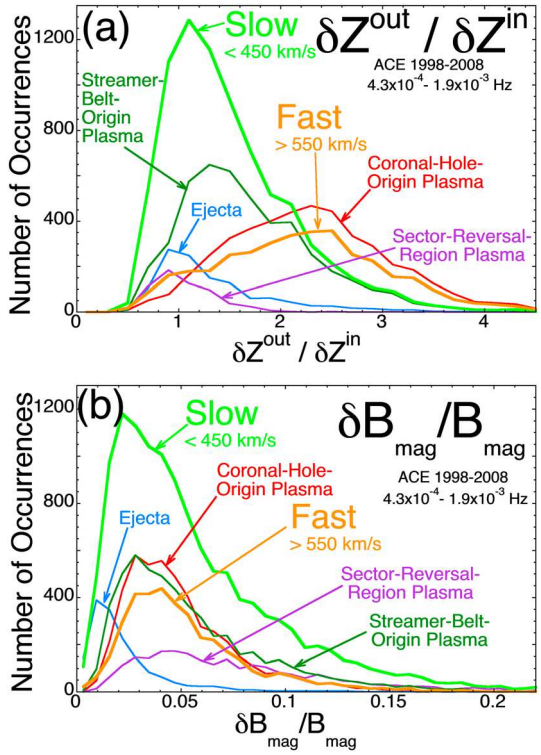


**Figure 17.** (a) The ratio of the Elsässer amplitudes of $Z^{out}$ and $Z^{in}$ in the frequency band $4.3 \times 10^{-4}$ to $1.9 \times 10^{-3}$ Hz and (b) the normalized root-mean-square amplitudes of magnetic field strength fluctuations in the frequency band $4.3 \times 10^{-4}$ to $1.9 \times 10^{-3}$ Hz are binned for the four types of plasma and for slow wind (defined as $v_{sw} < 450$ km/s) and fast wind (defined as $v_{sw} > 550$ km/s). The amplitudes are root-mean-square values of the Fourier-filtered 4.5-hr-long time series. The distributions in this plot are not equal-area normalized, rather they are the number of events in the data set.

Separating into plasma types is particularly important for slow solar wind. In Figure 17a the values of $\delta Z^{out}/\delta Z^{in}$ (cf. Figure 11a) for the 4.5-hr intervals of the ACE 1988–2008 data set are binned according to the four types of plasma and according to slow wind (taken here to be $v_{sw} \leq 450$ km/s; light-green curve) and fast wind (taken here to be $v_{sw} \geq 550$ km/s; orange curve). Note that the occurrence is plotted as the number of 4.5-hr intervals rather than the per cent of the values. Figure 17a demonstrates that the "slow wind" categorization misses the systematic differences in the outward-versus-inward imbalance between the unbalanced streamer-belt-origin plasma and the balanced sector-reversal-region plasma and ejecta. In Figure 17b the values of $\delta B_{mag}/B_{mag}$ (cf. Figure 16a) for the ACE 1998–2008 4.5-hr intervals are binned for the four types of plasma and for slow and fast wind. Note that the distribution of $\delta B_{mag}/B_{mag}$ values is about the same in "slow" wind as it is in "fast" wind, whereas the 3D4CAT categorization shows statistical differences in the $\delta B_{mag}/B_{mag}$ values for the four different plasma types. In Figure 17b the slow wind categorization misses the systematic differences of $\delta B_{mag}/B_{mag}$ between ejecta with very low values, streamer-belt-origin plasma with medium values, and sector-reversal-region plasma with higher values.

One safe exception to the problems of the slow-versus-fast categorization is when long intervals of fast Alfvénic plasma with nearly constant speed are investigated (e.g., Borovsky, 2016; Perri et al., 2011; Yordanova et al., 2009), particularly out of the ecliptic plane over a polar coronal hole (e.g., Goldstein et al., 1995; Neugebauer et al., 1997; Podesta & Gary, 2011; Wawrzaszek & Macek, 2010): such intervals are almost certainly purely coronal-hole-origin plasma.

### 12.2. The Origin of Differences Between the Four Types of Plasma

The four types of plasmas have different regions of origin on the Sun: this undoubtedly accounts for some of the systematic differences in the properties of the four plasmas and the differences in the properties of the fluctuations in the 4 plasmas.

One key difference in the fout types of plasma is the Parker spiral versus non-Parker spiral orientation of the magnetic field and the related open flux versus closed or disconnected flux natures of the magnetic field. A Parker spiral magnetic field is expected for plasma that is continuously emitted from an open-field spot on the solar surface (Hundhausen, 1972; Parker, 1958). Coronal-hole-origin plasma and streamer-belt-origin plasma have Parker spiral-oriented magnetic fields; they also have unidirectional electron strahls (Xu & Borovsky, 2015), indicating that they are on open magnetic field lines connected to the Sun. Impulsive plasma emissions, particularly from closed-field regions, are not expected to have Parker spiral-oriented magnetic fields. Large-scale ejecta are certainly impulsive (Richardson & Cane, 1996; Webb, 1991). The smaller-scale blobby emissions from streamer stalks are also impulsive (Foullon et al., 2011; Viall & Vourlidas, 2015; Wang et al., 2000). Ejecta tends to have a bidirectional electron strahl (Gosling et al., 1987; Skoug et al., 2000), indicating that the magnetic-field of the plasma has two foot points connected to the Sun. Sector-reversal-region plasma tends to have an absence of an electron strahl or an intermittent electron strahl (Xu & Borovsky, 2015), indicating that the plasma is at times magnetically disconnected from the Sun.

These related differences (1) open flux versus not open flux and (2) continuous versus impulsive emission may help to explain some of the systematic differences in the plasma fluctuations found in the present study. In Table 1 two extremes (e.g., smallest and largest, shallowest and steepest) are listed in a row 17 times. Of those 17 times, one extreme is in coronal-hole-origin plasma (open flux, continuous emission) and the other is in either sector-reversal-region plasma or ejecta (not open flux, impulsive emission). In the other 4 times out of 17 the two extremes are between ejecta and sector-reversal-region plasma.

The Parker spiral plasmas (coronal-hole-origin plasma and streamer-belt-origin plasma) tend to be more Alfvénic, with correlations between the vector velocity fluctuations and the vector magnetic-field fluctuations. Alfvénic fluctuations in the solar wind seem to be a sign of an open-flux process, perhaps reconnection events between open field lines and low-lying closed loops (Burkholder et al., 2019; He et al., 2010; Pariat et al., 2010; Shibata et al., 2007; Torok et al., 2009; Yang et al., 2013) or perhaps firehose instabilities driven by plasma jetting in open flux tubes (Farahani et al., 2009; Mann et al., 1992; Zhelyazkov, 2010).

Note that Figure 10 of Xu and Borovsky (2015), which plots the carbon-charge-state number density ratio $C^{6+}/C^{5+}$ versus the oxygen-charge-state number density $O^{7+}/O^{6+}$ of the solar wind at 1 AU, shows one trend for coronal-hole-origin plasma and streamer-belt-origin plasma (the open-flux plasmas) and a different trend for sector-reversal-region plasma and ejecta (the impulsive, nonopen-flux plasmas). See also the very similar Figure 2 of D'Amicis et al. (2019) where solar wind plasma at 1 AU is separated according to its Alfvénicity.

**Acknowledgments**
The authors thank John Podesta for useful conversations. Work at the Space Science Institute was supported by the NASA Heliophysics Guest Investigator Program via grant NNX17AB71G, by the NSF Solar-Terrestrial Program via grant AGS-12GG13659, by the NSF SHINE program via award AGS-1723416, by the NASA Heliophysics LWS program via grants NNX16AB75G, NNX14AN90G, NNX16AB83G, and 80NSSC17K0682, and by the NSF GEM Program. Work at the University of New Hampshire was supported by a subcontract from the California Institute of Technology in support of the ACE/MAG instrument. The ACE Hourly Data Parameters for Magnetospheric Driving data set was created with funding from the NASA Research in the Structure of the Solar Wind at 1 AU (RSSW@1 AU) Program. All measurements used are from the "Merged IMF and Solar Wind 64-second Averages" ACE data set available at http://www.srl.caltech.edu/ACE/ASC/level2/index.html and from the "ACE Hourly Data Parameters for Magnetospheric Driving" data set available at http://www.ssg.sr.unh.edu/mag/ace/HourlyParms/HourlyParms.html.

## References

Antiochos, S. K., Mikic, Z., Titov, V. S., Lionello, R., & Linker, J. A. (2011). A model for the sources of the slow solar wind. *The Astrophysical Journal*, *731*(2), 112. https://doi.org/10.1088/0004-637X/731/2/112

Arge, C. N., Odstrcil, D., Pizzo, V. J., & Mayer, L. R. (2003). Improved method for specifying solar wind speed near the Sun. *AIP Conference Proceedings*, *679*, 190.

Bavassano, B., Woo, R., & Bruno, R. (1997). Heliospheric plasma sheet and coronal streamers. *Geophysical Research Letters*, *24*(13), 1655–1658. https://doi.org/10.1029/97GL01630

Belcher, J. W., & Davis, L. (1971). Large amplitude Alfvén waves in the interplanetary medium, 2. *Journal of Geophysical Research*, *76*(16), 3534–3563. https://doi.org/10.1029/JA076i016p03534

Bendat, J. S., & Piersol, A. G. (1971). *Random data: Analysis and measurement procedures*, sect. 4.8.1. New York: John Wiley.

Bevington, P. R., & Robinson, D. K. (1992). *Data reduction and error analysis for the physical sciences* (2nd ed.). New York: McGraw-Hill.

Beyer, W. H. (1966). *Handbook of tables for probability and statistics*, *Sect. IX, Chem*. Cleveland, Ohio: Rubber.

Boldyrev, S., Perez, J. C., Borovsky, J. E., & Podesta, J. J. (2011). Spectral scaling laws in magnetohydrodynamic turbulence simulations and in the solar wind. *The Astrophysical Journal Letters*, *741*(1), L19. https://doi.org/10.1088/2041-8205/741/1/L19

Borovsky, J. E. (2008). The flux-tube texture of the solar wind: Strands of the magnetic carpet at 1 AU? *Journal of Geophysical Research*, *113*, A08110. https://doi.org/10.1029/2007JA012684

Borovsky, J. E. (2010a). On the variations of the solar-wind magnetic field about the Parker-spiral direction. *Journal of Geophysical Research*, *115*, A09101. https://doi.org/10.1029/2009JA015040

Borovsky, J. E. (2010b). On the contribution of strong discontinuities to the power spectrum of the solar wind. *Physical Review Letters*, *105*(11), 111102. https://doi.org/10.1103/PhysRevLett.105.111102

Borovsky, J. E. (2012a). The velocity and magnetic-field fluctuations of the solar wind at 1 AU: Statistical analysis of Fourier spectra and correlations with plasma properties. *Journal of Geophysical Research*, *117*, A05104. https://doi.org/10.1029/2011JA017499

Borovsky, J. E. (2012b). The effect of sudden wind shear on the Earth's magnetosphere: Statistics of wind-shear events and CCMC simulations of magnetotail disconnections. *Journal of Geophysical Research*, *117*, A06224. https://doi.org/10.1029/2012JA017623

Borovsky, J. E. (2016). The plasma structure of coronal hole solar wind: Origins and evolution. *Journal of Geophysical Research: Space Physics*, *121*, 5055–5087. https://doi.org/10.1002/2016JA022686

Borovsky, J. E. (2018). On the origins of the intercorrelations between solar wind variables. *Journal of Geophysical Research: Space Physics*, *123*(1), 20–29. https://doi.org/10.1002/2017JA024650

Borovsky, J. E., & Denton, M. H. (2010). Solar-wind turbulence and shear: A superposed-epoch analysis of corotating interaction regions at 1 AU. *Journal of Geophysical Research*, *115*, A10101. https://doi.org/10.1029/2009JA014966

Borovsky, J. E., & Denton, M. H. (2016). The trailing edges of high-speed streams at 1 AU. *Journal of Geophysical Research: Space Physics*, *121*, 6107–6140. https://doi.org/10.1002/2016JA022863

Borovsky, J. E., & Podesta, J. J. (2015). Exploring the effect of current sheet thickness on the high-frequency Fourier spectrum breakpoint of the solar wind. *Journal of Geophysical Research: Space Physics*, *120*, 9256–9268. https://doi.org/10.1002/2015JA021622

Bruno, R., Bavassano, B., Pietropaulo, E., Carbone, V., & Veltri, P. (1999). Effects of intermittency on interplanetary velocity and magnetic field fluctuation anisotropy. *Geophysical Research Letters*, *26*(20), 3185–3188. https://doi.org/10.1029/1999GL010668

Bruno, R., Carbone, V., Sorriso-Valvo, L., & Bavassano, B. (2003). Radial evolution of solar wind intermittency in the inner heliosphere. *Journal of Geophysical Research*, *108*(A3), 1130. https://doi.org/10.1029/2002JA009615

Bruno, R., & Trenchi, L. (2014). Radial dependence of the frequency break between fluid and kinetic scales in the solar wind fluctuations. *The Astrophysical Journal Letters*, *787*(2), L24. https://doi.org/10.1088/2041-8205/787/2/L24

Burkholder, B. L., Otto, A., Delamere, P. A., & Borovsky, J. E. (2019). Magnetic connectivity in the corona as a source of structure in the solar wind. *Journal of Geophysical Research: Space Physics*, *124*(1), 32–49. https://doi.org/10.1029/2018JA026132

Burlaga, L., Fitzenreiter, R., Lepping, R., Ogilvie, K., Szabo, A., Lazarus, A., et al. (1998). A magnetic cloud containing prominence material: January 1997. *Journal of Geophysical Research*, *103*(A1), 277–285. https://doi.org/10.1029/97JA02768

Burlaga, L., Sittler, E., Mariani, F., & Schwenn, R. (1981). Magnetic loop behind an interplanetary shock: Voyager, Helios, and IMP 8 observations. *Journal of Geophysical Research*, *80*, 6673.

Camporeale, E., Care, A., & Borovsky, J. E. (2017). Classification of solar wind with machine learning. *Journal of Geophysical Research: Space Physics*, *122*, 10,910–10,920. https://doi.org/10.1002/2017JA024383

Cane, H. V., & Richardson, I. G. (2003). Interplanetary coronal mass ejections in the near-Earth solar wind during 1996–2002. *Journal of Geophysical Research*, *108*(A4), 1156. https://doi.org/10.1029/2002JA009817

Carbone, V., Bruno, R., Sorriso-Valvo, L., & Lepreti, F. (2004). Intermittency of magnetic turbulence in slow solar wind. *Planetary and Space Science*, *52*(10), 953–956. https://doi.org/10.1016/j.pss.2004.02.005

Chen, C. H. K., Bale, S. D., Salem, C. S., & Maruca, B. A. (2013). Residual energy spectrum of solar wind turbulence. *Astrophysical Journal*, *770*(2), 125. https://doi.org/10.1088/0004-637X/770/2/125

Cranmer, S. R., Gibson, S. E., & Riley, P. (2017). Origins of the ambient solar wind: Implications for space weather. *Space Science Review*, *212*(3-4), 1345–1384. https://doi.org/10.1007/s11214-017-0416-y

Crooker, N. U., Antiochos, S. K., Zhao, X., & Neugebauer, M. (2012). Global network of slow solar wind. *Journal of Geophysical Research*, *117*, A04104. https://doi.org/10.1029/2011JA017236

Crooker, N. U., Huang, C.-L., Lamassa, S. M., Larson, D. E., Kahler, S. W., & Spence, H. E. (2004). Heliospheric plasma sheets. *Journal of Geophysical Research*, *109*, A03107. https://doi.org/10.1029/2003JA010170

Crooker, N. U., McPherron, R. L., & Owens, M. J. (2014). Comparison of interplanetary signatures of streamers and pseudostreamers. *Journal of Geophysical Research: Space Physics*, *119*, 4157–4163. https://doi.org/10.1002/2014JA020079

D'Amici, R., Matteini, L., & Bruno, R. (2016). Characterizing the Alfvénic slow wind: A case study. *AIP Conference Proceedings*, *1720*, 04002.

D'Amici, R., Matteini, L., & Bruno, R. (2019). On the slow solar wind with high Alfvénicity: From composition and microphysics to spectral properties. *Monthly Notices of the Royal Astronomical Society*, *483*, 4665.

D'Amicis, R., & Bruno, R. (2015). On the origin of highly Alfvénic slow solar wind. *The Astrophysical Journal*, *805*(1), 84. https://doi.org/10.1088/0004-637X/805/1/84

Elliott, H. A., McComas, D. J., Schwadron, N. A., Gosling, J. T., Skoug, R. M., Gloeckler, G., & Zurbuchen, T. H. (2005). An improved expected temperature formula for identifying ICMEs. *Journal of Geophysical Research*, *110*, A04103. https://doi.org/10.1029/2006JA011636

Farahani, S. V., Van Doorsselaere, T., Verwichte, E., & Nakariakov, V. M. (2009). Propagating transverse waves in soft x-ray coronal jets. *Astronomy & Astrophysics*, *498*(2), L29–L32. https://doi.org/10.1051/0004-6361/200911840

Fisk, L. A., Zurbuchen, T. H., & Schwadron, N. A. (1999). Coronal magnetic field: Consequences of large-scale motion. *The Astrophysical Journal*, *521*(2), 868–877. https://doi.org/10.1086/307556

Foullon, C., Lavraud, B., Luhmann, J. G., Farrugia, C. J., Retino, A., Simunac, K. D. C., et al. (2011). Plasmoid releases in the heliospheric current sheet and associated coronal hole boundary layer evolution. *The Astrophysical Journal*, *737*, 1.

Gary, S. P. (1999). Collisionless dissipation wavenumber: Linear theory. *Journal of Geophysical Research*, *104*(A4), 6759–6762. https://doi.org/10.1029/1998JA900161

Gary, S. P., & Borovsky, J. E. (2004). Alfvén-cyclotron fluctuations: Linear Vlasov theory. *Journal of Geophysical Research*, *109*, A06105. https://doi.org/10.1029/2004JA010399

Gary, S. P., & Borovsky, J. E. (2008). Damping of long-wavelength kinetic Alfvén fluctuations: Linear theory. *Journal of Geophysical Research*, *113*, A12104. https://doi.org/10.1029/2003JA010239

Goldstein, B. E., Smith, E. J., Balough, A., Horbury, T. S., Goldstein, M. L., & Roberts, D. A. (1995). Properties of magnetohydrodynamic turbulence in the solar wind as observed by Ulysses at high heliographic latitudes. *Geophysical Research Letters*, *22*(23), 3393–3396. https://doi.org/10.1029/95GL03183

Goldstein, M. L., Burlaga, L. F., & Matthaeus, W. H. (1984). Power spectral signatures of interplanetary corotating and transient flows. *Journal of Geophysical Research*, *89*(A6), 3747. https://doi.org/10.1029/JA089iA06p03747

Gosling, J. T., Baker, D. N., Bame, S. J., Feldman, W. C., Zwickl, R. D., & Smith, E. J. (1987). Bidirectional solar wind electron heat flux events. *Journal of Geophysical Research*, *92*(A8), 8519. https://doi.org/10.1029/JA092iA08p08519

Gosling, J. T., Borrini, G., Asbridge, J. R., Bame, S. J., Feldman, W. C., & Hansen, R. T. (1981). Coronal streamers in the solar wind at 1 AU. *Journal of Geophysical Research*, *86*(A7), 5438. https://doi.org/10.1029/JA086iA07p05438

Gosling, J. T., Pizzo, V., & Bame, S. J. (1973). Anomalously low proton temperatures in the solar wind following interplanetary shock waves—Evidence for magnetic bottles. *Journal of Geophysical Research*, *78*(13), 2001–2009. https://doi.org/10.1029/JA078i013p02001

Hadid, L. Z., Sahraoui, F., & Galtier, S. (2017). Energy cascade rate in compressible fast and slow wind turbulence. *The Astrophysical Journal*, *838*(1), 9. https://doi.org/10.3847/1538-4357/aa603f

He, J.-S., Tu, C.-Y., Tian, H., & Marsch, E. (2010). Solar wind origins in coronal holes and in the quiet Sun. *Advances in Space Research*, *45*(2), 303–309. https://doi.org/10.1016/j.asr.2009.07.020

Horbury, T. S., Forman, M. A., & Oughton, S. (2005). Spacecraft observations of solar wind turbulence: An overview. *Plasma Physics and Controlled Fusion*, *47*(12B), B703–B717. https://doi.org/10.1088/0741-3335/47/12B/S52

Howes, G. G., Cowley, S. C., Dorland, W., Hammett, G. W., Quataert, E., & Schekochihin, A. A. (2008). A model of turbulence in magnetized plasmas: Implications for the dissipation range in the solar wind. *Journal of Geophysical Research*, *113*, A05103. https://doi.org/10.1029/2007JA012665

Hundhausen, A. J. (1972). *Coronal expansion and solar wind*, sect. 1.5. Berlin: Springer-Verlag.

King, J. H., & Papitashvili, N. E. (2005). Solar wind spatial scales in and comparisons of hourly Wind and ACE plasma and magnetic field data. *Journal of Geophysical Research*, *110*, A02104. https://doi.org/10.1029/2004JA010649

Ko, Y. K., Roberts, D. A., & Lepri, S. T. (2018). Boundary of the slow solar wind. *The Astrophysical Journal*, *864*(2), 139. https://doi.org/10.3847/1538-4357/aad69e

Lavraud, B., & Borovsky, J. E. (2008). Altered solar wind-magnetosphere interaction at low Mach numbers: Coronal mass ejections. *Journal of Geophysical Research*, *113*, A00B08. https://doi.org/10.1029/2008JA013192

Leamon, R. J., Smith, C. W., Ness, N. F., Matthaeus, W. H., & Wong, H. K. (1998). Observational constraints on the dynamics of the interplanetary magnetic field dissipation range. *Journal of Geophysical Research*, *103*(A3), 4775–4787. https://doi.org/10.1029/97JA03394

Leamon, R. J., Smith, C. W., Ness, N. F., & Wong, H. K. (1999). Dissipation range dynamics: Kinetic Alfvén waves and the importance of $\beta_e$. *Journal of Geophysical Research*, *104*(A10), 22,331–22,344. https://doi.org/10.1029/1999JA900158

Lepping, R. P., Wu, C.-C., & Berdichevsky, D. B. (2005). Automatic identification of magnetic cloud-like regions at 1 AU: Occurrence rate and other properties. *Annales Geophysicae*, *23*(7), 2687–2704. https://doi.org/10.5194/angeo-23-2687-2005

Luhmann, J. G., Petrie, G., & Riley, P. (2013). Solar origins of solar wind properties during the cycle 23 solar minimum and rising phase of cycle 24. *Cairo University Journal of Advanced Research*, *4*(3), 221–228. https://doi.org/10.1016/j.jare.2012.08.008

Mann, G., Marsch, E., & Roberts, B. (1992). Surface and body waves in solar wind flow tubes. In E. Marsch & R. Schwenn (Eds.), *Solar wind seven*, COSPAR Colloquia Series (Vol. 3, p. 495). Oxford. Pergamon Press.

Marsch, E., & Tu, C.-Y. (1990a). On the radial evolution of MHD turbulence in the inner heliosphere. *Journal of Geophysical Research*, *95*(A6), 8211. https://doi.org/10.1029/JA095iA06p08211

Marsch, E., & Tu, C.-Y. (1990b). Spectral and spatial evolution of compressible turbulence in the inner solar wind. *Journal of Geophysical Research*, *95*(A8), 11945. https://doi.org/10.1029/JA095iA08p11945

McComas, D. J., Blame, S. J., Barker, P., Feldman, W. C., Phillips, J. L., Riley, P., & Griffee, J. W. (1998). Solar Wind Electron Proton Alpha Monitor (SWEPAM) for the advanced composition explorer. *Space Science Reviews*, *86*(1/4), 563–612. https://doi.org/10.1023/A:1005040232597

Neugebauer, M., Reisenfeld, D., & Richardson, I. G. (2016). Comparison of algorithms for determination of solar wind regimes. *Journal of Geophysical Research: Space Physics*, *121*, 8215–8227. https://doi.org/10.1002/2016JA023142

Neugebauer, M., Ruzmaikin, A., & McComas, D. J. (1997). Wavelet analysis of the structure of microstreams in the polar solar wind. *AIP Conference Proceedings*, *385*, 41. https://doi.org/10.1063/1.51765

Neugebauer, M., Steinberg, J. T., Tokar, R. L., Barraclough, B. L., Dors, E. E., Weins, R. C., et al. (2003). Genesis on-board determination of the solar wind flow regime. *Space Science Reviews*, *105*(3/4), 661–679. https://doi.org/10.1023/A:1024478129261

Pariat, E., Antiochos, S. K., & DeVore, C. R. (2010). Three-dimensional modeling of quasi-homologous solar jets. *The Astrophysical Journal*, *714*(2), 1762–1778. https://doi.org/10.1088/0004-637X/714/2/1762

Parker, E. N. (1958). Dynamics of the interplanetary gas and magnetic fields. *The Astrophysical Journal*, *128*, 664. https://doi.org/10.1086/146579

Perri, S., Carbone, V., Yordanova, E., Bruno, R., & Balough, A. (2011). Scaling law of the reduced magnetic helicity in fast streams. *Planetary and Space Science*, *59*(7), 575–579. https://doi.org/10.1016/j.pss.2010.04.017

Podesta, J. J. (2011). On the energy cascade rate of solar wind turbulence in high cross helicity flows. *Journal of Geophysical Research*, *116*, A05101. https://doi.org/10.1029/2010JA016306

Podesta, J. J. (2012). The need to consider ion Bernstein waves as a dissipation channel of solar wind turbulence. *Journal of Geophysical Research*, *117*, A07101. https://doi.org/10.1029/2012JA017770

Podesta, J. J. (2016). Spectra that behave like power-laws are not necessarily power-laws. *Advances in Space Research*, *57*(4), 1127–1132. https://doi.org/10.1016/j.asr.2015.12.020

Podesta, J. J., & Borovsky, J. E. (2016). Relationship between the durations of jumps in solar wind time series and the frequency of the spectral break. *Journal of Geophysical Research: Space Physics*, *121*, 1817–1838. https://doi.org/10.1002/2015JA021987

Podesta, J. J., Borovsky, J. E., & Gary, S. P. (2010). A kinetic Alfvén wave cascade subject to collisionless damping cannot reach electron scales in the solar wind at 1 AU. *The Astrophysical Journal*, *712*(1), 685–691. https://doi.org/10.1088/0004-637X/712/1/685

Podesta, J. J., & Gary, S. P. (2011). Magnetic helicity spectrum of solar wind fluctuations as a function of the angle with respect to the local mean magnetic field. *The Astrophysical Journal*, *734*(1), 15. https://doi.org/10.1088/0004-637X/734/1/15

Podesta, J. J., Roberts, D. A., & Goldstein, M. L. (2007). Spectral exponents of kinetic and magnetic energy spectra in solar wind turbulence. *The Astrophysical Journal*, *664*(1), 543–548. https://doi.org/10.1086/519211

Reisenfeld, D. B., Steinberg, J. T., Barraclough, B. L., Dors, E. E., Weins, R. C., Neugebauer, M., et al. (2003). Comparison of the Genesis solar wind regime algorithm results with solar wind composition observed by ACE. *AIP Conference Proceedings*, *679*, 632. https://doi.org/10.1063/1.1618674

Riazantseva, M. O., Zastenker, G. N., & Richardson, J. D. (2005). The characteristics of sharp (small-scale) boundaries of solar wind plasma and magnetic field structures. *Advances in Space Research*, *35*(12), 2147–2151. https://doi.org/10.1016/j.asr.2004.12.011

Richardson, I. G., & Cane, H. V. (1995). Regions of abnormally low proton temperature in the solar wind (1965–1991) and their association with ejecta. *Journal of Geophysical Research*, *100*(A12), 23397. https://doi.org/10.1029/95JA02684

Richardson, I. G., & Cane, H. V. (1996). Particle flows observed in ejecta during solar event onsets and their implication for the magnetic field topology. *Journal of Geophysical Research*, *101*(A12), 27521–27532. https://doi.org/10.1029/96JA02643

Richardson, I. G., & Cane, H. V. (2010). Near-Earth interplanetary coronal mass ejections during solar cycle 23: Catalog and summary of properties. *Solar Physics*, *264*(1), 189–237. https://doi.org/10.1007/s11207-010-9568-6

Roberts, O. W., Narita, Y., Li, X., Escoubet, C. P., & Laakso, H. (2017). Multipoint analysis of compressive fluctuations in the fast and slow solar wind. *Journal of Geophysical Research: Space Physics*, *122*, 6940–6963. https://doi.org/10.1002/2016JA023552

Sahraoui, F., Belmont, G., & Goldstein, M. L. (2012). New insight into short-wavelength solar wind fluctuations from Vlasov theory. *The Astrophysical Journal*, *748*(2), 100. https://doi.org/10.1088/0004-637X/748/2/100

Sahraoui, F., Goldstein, M. L., Belmont, G., Canu, P., & Rezeau, L. (2010). Three dimensional anisotropic *k* spectra of turbulence at sub-proton scales in the solar wind. *Physical Review Letters*, *105*(13), 131,101. https://doi.org/10.1103/PhysRevLett.105.131101

Saito, S., Gary, S. P., & Narita, Y. (2010). Wavenumber spectrum of whistler turbulence: Particle-in-cell simulation. *Physics of Plasmas*, *17*(12), 122316. https://doi.org/10.1063/1.3526602

Salem, C., Mangeney, A., Bale, S. D., & Veltri, P. (2009). Solar wind MHD turbulence: Anomalous scaling and role of intermittency. *The Astrophysical Journal*, *702*(1), 537–553. https://doi.org/10.1088/0004-637X/702/1/537

Schwenn, R. (1983). The "average" solar wind in the inner heliosphere: Structures and slow variations, in Solar Wind Five. *NASA Conference Publication*, *2280*, 489.

Shibata, K., Nakamura, T., Matsumoto, T., Otsuji, K., Okamoto, T. J., Nishizuka, N., et al. (2007). Chromospheric anemone jets as evidence of ubiquitous reconnection. *Science*, *318*(5856), 1591–1594. https://doi.org/10.1126/science.1146708

Siscoe, G. L., Davis, L., Coleman, P. J., Smith, E. J., & Jones, D. E. (1968). Power spectra and discontinuities of the interplanetary magnetic field: Mariner 4. *Journal of Geophysical Research*, *73*(1), 61–82. https://doi.org/10.1029/JA073i001p00061

Skoug, R. M., Feldman, W. C., Gosling, J. T., McComas, D. J., & Smith, C. W. (2000). Solar wind electron characteristics inside and outside coronal mass ejections. *Journal of Geophysical Research*, *105*(A10), 23069–23084. https://doi.org/10.1029/2000JA000017

Smith, C. W., Acuna, M. H., Burlaga, L. F., L'Heureux, J., Ness, N. F., & Scheifele, J. (1998). The ACE magnetic fields experiment. *Space Science Reviews*, *86*, 611.

Smith, C. W., Valquez, B. J., & Hamilton, K. (2006). Interplanetary magnetic fluctuation anisotropy in the inertial range. *Journal of Geophysical Research*, *111*, A09111. https://doi.org/10.1029/2006JA011651

Stansby, D., Horbury, T. S., & Matteini, L. (2018). Diagnosing solar wind origins using in situ measurements in the inner heliosphere. *Monthly Notices of the Royal Astronomical Society*, *482*, 1706.

Stawicki, O., Gary, S. P., & Li, H. (2001). Solar wind magnetic fluctuation spectra: Dispersion and damping. *Journal of Geophysical Research*, *106*(A5), 8273–8281. https://doi.org/10.1029/2000JA000446

Subramanian, S., Madjarska, M. S., & Doyle, J. G. (2010). Coronal hole boundaries evolution at small scales. *Astronomy & Astrophysics*, *516*(A50), A50. https://doi.org/10.1051/0004-6361/200913624

Suess, S. T., Ko, Y.-K., Von Steiger, R., & Moore, R. L. (2009). Quiescent current sheets in the solar wind and origins of slow wind. *Journal of Geophysical Research*, *114*, A04103. https://doi.org/10.1029/2008JA013704

Susino, R., Ventura, R., Spadaro, D., Vourlidas, A., & Landi, E. (2008). Physical parameters along the boundaries of a mid-latitude streamer and its adjacent regions. *Astronomy & Astrophysics*, *488*(1), 303–310. https://doi.org/10.1051/0004-6361:200809713

TenBarge, J. M., Podesta, J. J., Klein, K. G., & Howes, G. G. (2012). Interpreting magnetic variance anisotropy measurements in the solar wind. *The Astrophysical Journal*, *735*, 107.

Teodorescu, E., Echim, M., Munteanu, C., Zhang, T., Bruno, R., & Kovacs, P. (2015). Inertial range turbulence of fast and slow solar wind at 0.72 AU and solar minimum, *The. Astrophysical Journal Letters*, *804*(2), L41. https://doi.org/10.1088/2041-8205/804/2/L41

Tessein, J. A., Smith, C. W., MacBride, B. T., Matthaeus, W. H., Forman, M. A., & Borovsky, J. E. (2009). Spectral indices for multi-dimensional interplanetary turbulence at 1 AU. *The Astrophysical Journal*, *692*(1), 684–693. https://doi.org/10.1088/0004-637X/692/1/684

Tessein, J. A., Smith, C. W., Vasquez, B. J., & Skoug, R. M. (2011). Turbulence associated with corotating interaction regions at 1 AU: Inertial and dissipation range magnetic field spectra. *Journal of Geophysical Research*, *116*, A10104. https://doi.org/10.1029/2011JA016647

Torok, T., Aulanier, G., Schmieder, B., Reeves, K. K., & Golub, L. (2009). Fan-spine topology formation through two-step reconnection driven by twisted flux emergence. *The Astrophysical Journal*, *704*(1), 485–495. https://doi.org/10.1088/0004-637X/704/1/485

Tu, C.-Y., & Marsch, E. (1994). On the nature of compressive fluctuations in the solar wind. *Journal of Geophysical Research*, *99*(A11), 21481. https://doi.org/10.1029/94JA00843

Tu, C.-Y., & Marsch, E. (1995). MHD structures, waves and turbulence in the solar wind. *Space Science Reviews*, *73*(1-2), 1–210. https://doi.org/10.1007/BF00748891

Tu, C.-Y., Marsch, E., & Thieme, K. M. (1989). Basic properties of solar wind MHD turbulence near 0.3 AU analyzed by means of Elsässer variables. *Journal of Geophysical Research*, *94*(A9), 11739. https://doi.org/10.1029/JA094iA09p11739

Vasquez, B. J., Forman, M. A., Coburn, J. T., Smith, C. W., & Stawarz, J. E. (2018). The turbulent cascade for high cross-helicity states at 1 AU. II. Minor energy. *The Astrophysical Journal*, *867*(2), 156. https://doi.org/10.3847/1538-4357/aae6c6

Verscharen, D., Chen, C. H. K., & Wicks, R. T. (2017). On kinetic slow modes, fluid slow modes, and pressure-balanced structures in the solar wind. *Astrophysical Journal*, *840*(2), 106. https://doi.org/10.3847/1538-4357/aa6a56

Viall, N. M., & Vourlidas, A. (2015). Periodic density structures and the origin of the slow solar wind. *The Astrophysical Journal*, *807*(2), 176. https://doi.org/10.1088/0004-637X/807/2/176

Wang, X., Tu, C.-Y., He, J.-S., Wang, L.-H., Yao, S., & Zhang, L. (2018). Possible noise nature of Elsässer Variablez—In Highly Alfvénic solar wind fluctuations. *Journal of Geophysical Research: Space Physics*, *123*(1), 57–67. https://doi.org/10.1002/2017JA024743

Wang, Y.-M., & Sheeley, N. R. (1990). Solar wind speed and coronal flux-tube expansion. *The Astrophysical Journal*, *355*, 726. https://doi.org/10.1086/168805

Wang, Y.-M., Sheeley, N. R., Socker, D. G., Howard, R. A., & Rich, N. B. (2000). The dynamical nature of coronal streamers. *Journal of Geophysical Research*, *105*, 25,113.

Wawrzaszek, A., & Macek, W. M. (2010). Observation of the multifractal spectrum in solar wind turbulence by Ulysses at high latitudes. *Journal of Geophysical Research*, *115*, A07104. https://doi.org/10.1029/2009JA015176

Webb, D. F. (1991). The solar cycle variation of the rates of CMEs and related activity. *Advances in Space Research*, *11*(1), 37–40. https://doi.org/10.1016/0273-1177(91)90086-Y

Winterhalter, D., Neugebauer, M., Goldstein, B. E., Smith, E. J., Bame, S. J., & Balogh, A. (1994). Ulysses field and plasma observations of magnetic holes in the solar wind and their relation to mirror-mode structures. *Journal of Geophysical Research*, *99*(A12), 23371. https://doi.org/10.1029/94JA01977

Winterhalter, D., Smith, E. J., Burton, M. E., Murphy, N., & McComas, D. J. (1994). The heliospheric plasma sheet. *Journal of Geophysical Research*, *99*(A4), 6667. https://doi.org/10.1029/93JA03481

Xu, F., & Borovsky, J. E. (2015). A new four-plasma categorization scheme for the solar wind. *Journal of Geophysical Research: Space Physics*, *120*, 70–100. https://doi.org/10.1002/2014JA020412

Yang, L., He, J., Peter, H., Tu, C., Chen, W., Zhang, L., et al. (2013). Injection of plasma into the nascent solar wind via reconnection driven by supergranular advection. *The Astrophysical Journal*, *770*(6), 2013.

Yordanova, E., Balogh, A., Nouyllez, A., & von Steiger, R. (2009). Turbulence and intermittency in the heliospheric magnetic field in fast and slow wind. *Journal of Geophysical Research*, *114*, A08101. https://doi.org/10.1029/2009JA014067

Zhao, L., Zurbuchen, T. H., & Fisk, L. A. (2009). Global distribution of the solar wind during solar cycle 23: ACE observations. *Geophysical Research Letters*, *36*, L14104. https://doi.org/10.1029/2009GL039181

Zhelyazkov, I. (2010). Hall-magnetohydrodynamic waves in flowing ideal incompressible solar-wind plasmas. *Plasma Physics and Controlled Fusion*, *52*(6). https://doi.org/10.1088/0741-3335/52/6/065008